Evolution of ultrapotassic volcanism on the Kaapvaal craton: deepening the orangeite versus lamproite debate

Sebastian Tappe[1,2]*, Azhar M. Shaikh[1], Allan H. Wilson[3] and Andreas Stracke[4]

[1]Deep and Early Earth Processes Research Group, Department of Geology, University of Johannesburg, 2006 Auckland Park, South Africa

[2]Department of Geosciences, UiT – The Arctic University of Norway, N-9037, Tromsø, Norway

[3]School of Geosciences, University of the Witwatersrand, 2050 Johannesburg, South Africa

[4]Institut für Mineralogie, Westfälische Wilhelms-Universität, Corrensstrasse 24, 48149 Münster, Germany

ST, 0000-0003-1224-5155; AMS, 0000-0002-7327-5414

*Correspondence: sebastiant@uj.ac.za; sebastian.tappe@uit.no

Abstract: Orangeites are a significant source of diamonds, yet ambiguity surrounds their status among groups of mantle-derived potassic rocks. This study reports mineralogical and geochemical data for a *c.* 140 Ma orangeite dyke swarm that intersects the Bushveld Complex on the Kaapvaal craton in South Africa. The dykes comprise distinctive petrographic varieties that are linked principally by olivine fractionation, with the most evolved members containing minor amounts of primary carbonate, sanidine and andradite garnet in the groundmass. Although abundant groundmass phlogopite and clinopyroxene have compositions that are similar to those of cratonic lamproites, these phases show notable Ti-depletion, which we consider a hallmark feature of type orangeites from the Kaapvaal craton. Ti-depletion is also characteristic of bulk rock compositions and is associated with strongly depleted Th–U–Nb–Ta contents at high Cs–Rb–Ba–K concentrations. The resultant high large ion lithophile element/high field strength element ratios of orangeites suggest that mantle source enrichment occurred by metasomatic processes in the proximity of ancient subduction zones. The Bushveld-intersecting orangeite dykes have strongly enriched Sr–Nd–Hf isotopic compositions (initial $^{87}Sr/^{86}Sr = 0.70701–0.70741$; $\varepsilon Nd = -10.6$ to -5.8; $\varepsilon Hf = -14.4$ to -2.5), similar to those of other orangeites from across South Africa. Combined with the strong Ti–Nb–Ta depletion, this ubiquitous isotopic feature points to the involvement of ancient metasomatized mantle lithosphere in the origin of Kaapvaal craton orangeites, where K-rich metasomes imparted a 'fossil' subduction geochemical signature. Previous geochronology studies identified ancient K-enrichment events within the Kaapvaal cratonic mantle lithosphere, possibly associated with collisional tectonics during the 1.2–1.1 Ga Namaqua–Natal orogeny of the Rodinia supercontinent cycle. It therefore seems permissible that the cratonic mantle root was preconditioned for ultrapotassic magma production by tectonomagmatic events that occurred along convergent plate margins during the Proterozoic. However, reactivation of the K-rich metasomes had to await establishment of an extensional tectonic regime, such as that during the Mesozoic breakup of Gondwana, which was accompanied by widespread (1000 × 750 km) small-volume orangeite volcanism between 200 and 110 Ma. Although similarities exist between orangeites and lamproites, these and other potassic rocks are sufficiently distinct in their compositions such that different magma formation processes must be considered. In addition to new investigations of the geodynamic triggers of K-rich ultramafic magmatism, future research should more stringently evaluate the relative roles of redox effects and volatile components such as H_2O–CO_2–F in the petrogeneses of these potentially diamondiferous alkaline rocks.

Supplementary material: Mineral and bulk rock compositions including Sr–Nd–Hf isotope ratios are available at https://doi.org/10.6084/m9.figshare.c.5440652

The Kaapvaal craton in southern Africa is host to numerous occurrences of kimberlite, which traditionally have been divided into two groups based on petrographic characteristics and compositions: the so-called (1) archetypal Group 1 kimberlites and (2) highly micaceous Group 2 kimberlites, also known as 'orangeites' (Wagner 1914; Smith *et al.* 1985; Skinner 1989; Mitchell 1995). Group 1 kimberlite magmatism of the Kaapvaal craton and surrounding mobile belts has occurred repeatedly since at least 1800 Ma, with prominent eruption episodes at around 1150, 520, 240 and 90 Ma (Jelsma *et al.* 2009; Griffin *et al.* 2014; Tappe *et al.* 2018). Archetypal Group 1 kimberlites are both petrographically and geochemically relatively homogeneous, and their moderately depleted to slightly enriched

From: Krmíček, L. and Chalapathi Rao, N. V. (eds) *Lamprophyres, Lamproites and Related Rocks: Tracers to Supercontinent Cycles and Metallogenesis*. Geological Society, London, Special Publications, **513**, https://doi.org/10.1144/SP513-2021-84

Sr–Nd–Hf isotopic compositions suggest an origin from the convecting upper mantle (Smith 1983; Nowell *et al.* 2004; Tappe *et al.* 2020*a*, *b*). A convecting upper mantle origin is also consistent with the lack of anomalous ^{182}W abundances in these CO_2–H_2O-rich ultramafic magmas (Tappe *et al.* 2020*b*), which rules out significant melt contributions from lower mantle plumes to kimberlite magmatism, in contrast to many oceanic island basalt suites (Rizo *et al.* 2019; Mundl-Petermeier *et al.* 2020). The overwhelming majority of superlative diamond deposits are hosted by Group 1 kimberlites, not only across southern Africa but also on other cratons worldwide (Janse and Sheahan 1995; de Wit *et al.* 2016).

In contrast, Group 2 kimberlite *or* orangeite magmatism on the Kaapvaal craton and adjoining mobile belts appears to be temporally restricted to the Mesozoic between 200 and 110 Ma (Phillips *et al.* 1998; Griffin *et al.* 2014; Tappe *et al.* 2018), and its diamond potential is typically lower compared with that of Group 1 kimberlites (Field *et al.* 2008). Orangeites are a petrographically and geochemically heterogeneous group of potassic ultramafic rocks that can be reminiscent of cratonic lamproites or certain types of lamprophyres. Besides olivine-rich primitive varieties, there are several occurrences of more evolved olivine-poor orangeites that may contain groundmass sanidine or leucite (Mitchell 1995; Howarth *et al.* 2011). Extremely high large ion lithophile element (LILE) contents and the strongly enriched Sr–Nd–Hf isotopic compositions of orangeites are in stark contrast to archetypal kimberlites, and point to melt derivation from ancient K-metasomatized lithospheric mantle sources (Fraser *et al.* 1985; Nowell *et al.* 2004; Becker and le Roex 2006; Coe *et al.* 2008).

Compared with archetypal kimberlites, the mineralogy and geochemistry of type orangeite from the Kaapvaal craton are surprisingly poorly studied. For example, several decades of extensive platinum mining on the western lobe of the *c.* 2056 Ma Bushveld Complex exposed numerous highly micaceous ultramafic dykes that cut across the central Kaapvaal craton (Fig. 1), but there is a dearth of petrological information about these dykes in the public domain. They have been loosely referred to as 'micaceous' or 'lamprophyric' (Leeb-Du Toit 1986; Hughes *et al.* 2016; Daya 2019; Lerobane 2020), and most investigations have focussed on their geotechnical properties because these dykes are associated with life-threatening gas outbursts and tunnel failures in underground platinum mining operations (Daya *et al.* 2018; Moate 2019). Geochronology databases list the emplacement age of these diamond-poor to barren potassic ultramafic dykes on the western lobe of the Bushveld Complex at *c.* 140 Ma (Jelsma *et al.* 2009; Tappe *et al.* 2018). This suggests a genetic link to the *c.* 145 Ma diamondiferous orangeite dyke swarm near Swartruggens (Mitchell 1995), which is located *c.* 60 km west of the Bushveld Complex and is host to Helam Diamond Mine (Gurney and Kirkley 1996; McKenna *et al.* 2004; Field *et al.* 2008; Fig. 1).

In this contribution, we present a detailed account on the mineralogy and geochemistry, including Sr–Nd–Hf isotope data, of the potassic ultramafic dykes from the western Bushveld Complex, sampled at the Impala and Sibanye–Stillwater platinum mine leases near Rustenburg in 2019 (Figs 1 & 2). Our data show that these dyke occurrences represent typical Group 2 kimberlites *or* orangeites, many of which are compositionally evolved, suggesting petrographic resemblance to ultramafic lamprophyres. Although olivine fractionation was the key driver in the evolution of the orangeite magmatic system on the central Kaapvaal craton, it remains unclear why this process was apparently much more efficient compared with orangeite magmatism on the western Kaapvaal craton (Mitchell 1995). The case of the mostly barren Mesozoic orangeite dykes transecting the western Bushveld Complex provides a tangible example of how the diamond potential of potassic ultramafic magmas can rapidly diminish upon ascent – opening further new research avenues into this commercially relevant topic.

Kaapvaal craton and Bushveld Complex: an overview

The Kaapvaal craton in southern Africa presents one of the best preserved remnants of an Archean continent (de Wit *et al.* 1992; Kröner *et al.* 2019). Its rock record dates back to *c.* 3.66 Ga and vestiges of Hadean proto-crust have recently been identified in detrital zircon populations from the Early Archean Barberton Supergroup (Byerly *et al.* 2018). On the basis of its Archean geological evolution, the Kaapvaal craton has traditionally been divided into four geographical domains (i.e. eastern, northern, western, central) comprising typical granite–greenstone rock assemblages (Poujol *et al.* 2003), which amalgamated into a larger proto-continent during the Late Archean (Shirey *et al.* 2002; Smart *et al.* 2016). The central and eastern domains form the Witwatersrand block, which grew by magmatic and tectonic accretion between 3.6 and 3 Ga, as opposed to the younger Kimberley block (3.0–2.7 Ga) that comprises large parts of the western Kaapvaal craton (Schmitz *et al.* 2004). Late Archean cratonization of the Kaapvaal lithosphere was complete by 2.7 Ga, accompanied by the development of large cratonic basins (e.g. the 'Supergroups' filling the Pongola, Witwatersrand and Ventersdorp basins), which were to some extent rift-related

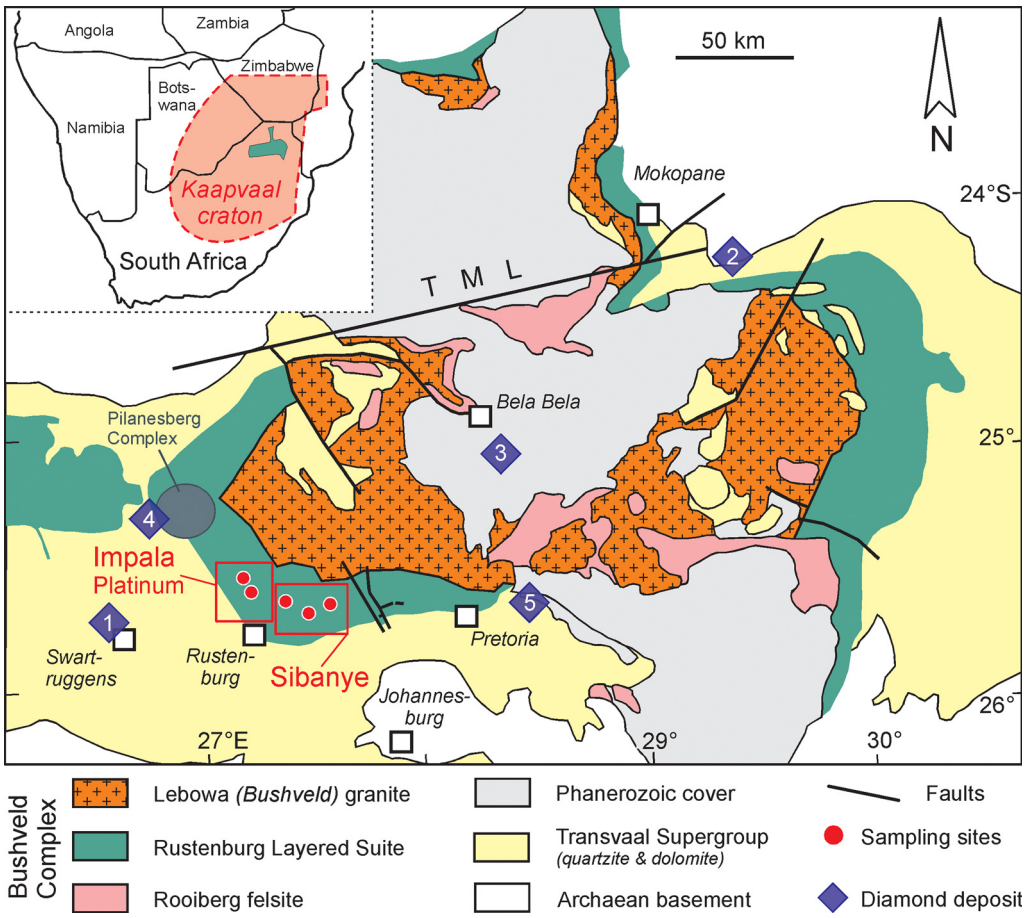

Fig. 1. Geological overview map of the *c.* 2056 Ma Bushveld Complex and surrounding areas on the central Kaapvaal craton in South Africa (modified from Zeh *et al.* 2019). The inset shows the location of the Kaapvaal craton in southern Africa. The *c.* 140 Ma orangeite dyke swarm on the western lobe of the Bushveld Complex is mainly exposed in the underground mines of the Impala Platinum Holdings Limited and Sibanye–Stillwater Limited leases near Rustenburg. A *c.* 145 Ma orangeite dyke system is mined for diamonds near the town of Swartruggens some 60 km west of the Bushveld Complex. TML, Thabazimbi–Murchison Lineament. Primary diamond deposits at: (1) 'Swartruggens/Helam' in a *c.* 145 Ma orangeite dyke system; (2) 'Klipspringer–Marsfontein' in a *c.* 155 Ma orangeite dyke–blow system; (3) 'Palmietgat' in *c.* 160 Ma kimberlite pipes; (4) 'Palmietfontein in a *c.* 75 Ma kimberlite pipe; and (5) 'Premier/Cullinan' in a *c.* 1150 Ma kimberlite pipe (the ages are after Griffin *et al.* 2014; Tappe *et al.* 2018; Smart *et al.* 2021).

(Frimmel *et al.* 2009; Agangi *et al.* 2020; Gumsley *et al.* 2020). The Kaapvaal craton was mostly submerged below sea-level between 2.65 and 2 Ga when deposition of the >10 km thick Transvaal Supergroup occurred. At *c.* 2056 Ma, the Transvaal basinal rock succession was intruded by the giant Bushveld Complex on the central Kaapvaal craton (Zeh *et al.* 2015, 2019).

The 400 × 300 × 9 km saucer-shaped Bushveld Complex presents the largest known continental layered mafic intrusion, but it also includes significant volumes of felsic rocks such as the vast Lebowa granite suite and Rooiberg Group (Cawthorn *et al.* 2006; Fig. 1). The Rustenburg Layered Suite, up to 9 km thick, comprises various types of mafic–ultramafic cumulate rocks, with numerous relatively thin mineralized layers that form chromite and platinum-group-mineral-enriched zones commonly referred to as 'reefs', exploited on the three main lobes of the Bushveld Complex (i.e. western, eastern and northern lobes; Fig. 1). The pyroxenitic–anorthositic Merensky Reef and underlying UG2 chromitite reef represent world's largest proven ore reserves of Pt–Pd–Rh and Cr, currently extracted in numerous

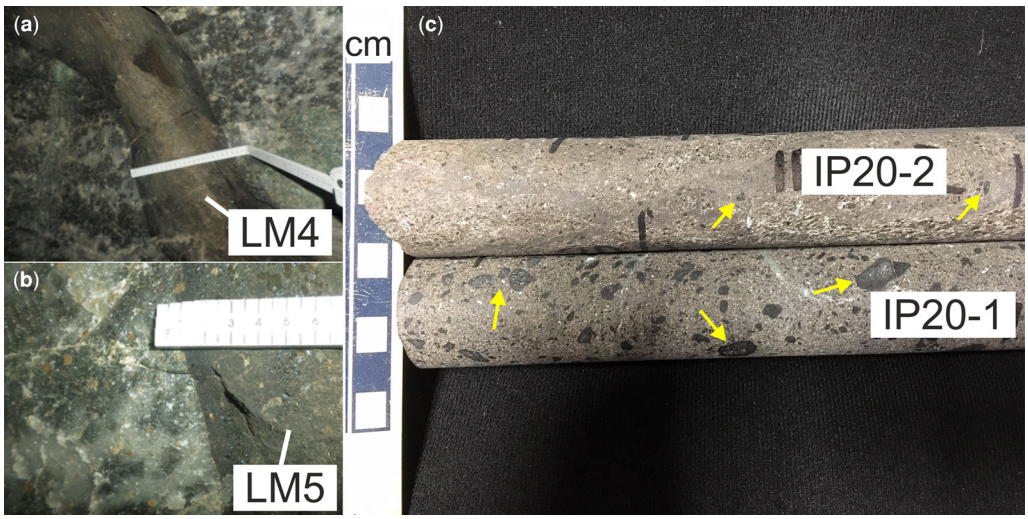

Fig. 2. Typical orangeite dyke exposures in underground mining tunnels and exploration drillcore intersections. (**a**, **b**) Approximately 0.2 m wide, near-vertical orangeite dykes exposed in the vicinity of the Merensky Reef at Karee-3 Shaft (samples LM4 and LM5). Note the sharp contacts against footwall anorthosites of the Critical Zone of the Rustenburg Layered Suite. (**c**) Characteristic micaceous drillcore intersections of so-called olivine-rich (IP20-1) and olivine-poor *or* evolved (IP20-2) orangeite dykes in the vicinity of Impala Shaft-20. The arrows point at relatively abundant olivine macrocrysts that are mostly serpentinized.

underground mining operations between 300 and 1000 m depth below the surface. On the western lobe of the Bushveld Complex, these mining activities exposed a diamond-poor to barren swarm of thin potassic ultramafic dykes of Mesozoic age that forms the subject of this study (Fig. 2).

Methodology

Acquisition and preparation of samples

Fifteen discrete 0.1–1 m wide potassic ultramafic dykes were sampled on the western lobe of the Bushveld Complex near Rustenburg during the course of 2019 (Figs 1 & 2). The samples are derived from the underground mining operations and exploration drilling activities of Impala Platinum (Shaft-20 and surrounding areas, $n = 11$) and Sibanye–Stillwater (formerly Lonmin Platinum Limited, Saffy and Karee-3 shafts, $n = 4$). Underground sampling of the dykes occurred in production tunnels at variable depth levels in footwall drives to the Merensky and UG2 ore reefs, *c.* 800–1000 m below the surface (Fig. 2).

The freshest samples were cut into thin slabs with a rock saw and small blocks were used for the preparation of polished petrographic thin sections at the University of Johannesburg, South Africa. The rock slabs were washed under running water and only materials visibly free from crust-derived rock fragments were processed further. The rock slabs (*c.* 250 g per sample) were then wrapped in thick plastic sleeves and crushed with a hammer into <8 mm large chips. Approximately 100 g of rock chips per sample were then processed in an agate mill at the University of Johannesburg to obtain analytical grade powder.

Electron microprobe analysis

Quantitative major and minor element analysis of rock-forming minerals was conducted on representative thin sections employing a Cameca SX100 electron probe micro-analyser at the University of Johannesburg. The polished thin sections were covered with *c.* 25 nm thick carbon layers under vacuum in a Quorum Q3OOT ES coater. The electron microprobe instrument was calibrated using a variety of natural standards: jadeite (Na), olivine (Mg), almandine (Al), diopside (Si), orthoclase (K), wollastonite (Ca), rhodonite (Mn), hematite (Fe), barite (Ba), fluorite (F) and halite (Cl). Synthetic pure metal oxides were used as calibration standards for Ti, Cr and Ni. Chemical elements of interest were measured on their respective X-ray K_α lines, and matrix corrections were performed with the 'X-PHI' method, which is a $\varphi(\rho z)$ offline correction routine. The lower limit of detection for the quantified major and minor element abundances is *c.* 0.05 wt%. The diverse mineralogy of the potassic ultramafic dykes required different electron

probe micro-analyser setups for 'dry' phases (e.g. olivine, diopside, spinel-group minerals) and 'volatile-bearing' phases (e.g. phlogopite). Therefore, the electron beam parameters and element signal counting times varied between setups. For example, the electron beam acceleration voltage was adjusted to 15 kV for phlogopite analyses, whereas 20 kV was applied during analysis of the 'dry' phases. The electron beam current was adjusted to 20 nA for both analytical routines. Peak intensity counting times varied between 10 and 60 s depending on the chemical element of interest. The electron beam diameter for spot analysis varied between setups: i.e. 1 μm for 'dry' and 2 μm for 'volatile-bearing' phases. The in-house almandine-rich garnet (Alma-PH1) and diopside-rich clinopyroxene (Diop-PH1) standards were repeatedly analysed during this study to monitor data accuracy and precision (Ngwenya and Tappe 2021).

X-ray fluorescence analysis and CO_2 determination

Bulk rock major and minor element concentrations were determined with a PANalytical MagiX PRO X-ray fluorescence spectrometer (XRF) at the University of Johannesburg. Sample powders were dried in an oven at 105°C prior to fusion into glass discs with a $Li_2B_4O_7$–$LiBO_2$ flux. The XRF method detection limit is *c.* 0.05 wt% for all chemical elements reported in Table 1. Instrument calibration was conducted with mixtures of pure metal oxides, and the accuracy of the XRF method was monitored by analysis of certified reference materials (BE-N, JSy-1, SARM-2, SARM-16), as well as analysis of carbonatite ST199 and kimberlite ST220II in-house standards (Dongre and Tappe 2019). For the in-house standards, all major and minor elements reported in Table 1 and Supplementary Material 1 were reproduced within 3% and typically better than 1% of the values listed in Tappe *et al.* (2006), except for MnO (better than 8%), Na_2O (12%) and K_2O (6%). Loss on ignition was determined after heating of the sample powders to 930°C in air and holding at this temperature for 30 min.

Bulk rock CO_2 contents were determined at the University of Münster (Germany) by liberation of CO_2 gas from the powders in a reaction with H_3PO_4. Liberated CO_2 gas was then cryogenically purified and collected into break-seal Pyrex tubes. The sample CO_2 concentrations were determined relative to a natural carbonate standard using a Thermo-Finnigan Delta Plus gas source mass spectrometer fitted with a dual inlet. The detection limit for the CO_2 concentration measurements was 0.01 wt% (Table 1).

Inductively coupled plasma mass spectrometry

Sample powder digestion for trace element inductively coupled plasma mass spectrometry (ICP-MS) analysis was undertaken at the University of the Witwatersrand in Johannesburg. Approximately 50 mg of rock powder per sample were loaded into microwave Teflon vessels. Concentrated HF-HNO_3 (6 ml) was added to each vessel, and powders were dissolved in a MARS microwave digester for 60 min. The sample solutions were then transferred to 15 ml Savillex beakers, which were placed on a hotplate at 60°C for 24 h and subsequently dried down at 70°C. Approximately 2 ml HNO_3 were then added to each beaker, and the previous heating step was repeated twice. Trace element analysis was performed with a Perkin Elmer ELAN Drc-e Q-ICP-MS instrument. Internal standards were Rh, Re, In and Bi, and ICP-MS calibration standards were made from certified solutions (Wilson 2012). During this study, replicate analyses of the USGS basaltic reference material BHVO-2 (Jochum *et al.* 2016) and the Mintek kimberlite reference material SARM-39 (Roy *et al.* 2007; Tappe *et al.* 2020*a*) yielded trace element concentrations within 10% of the recommended values, excluding Gd, Tm, Nb and Ta (within 20%).

Sr–Nd–Hf isotope ratio measurements

Purification of bulk rock Sr, Nd and Hf cuts for isotope ratio measurements was achieved through ion exchange chromatography at the University of Münster, and detailed descriptions of the clean-laboratory and mass spectrometry methods are provided in Tappe *et al.* (2020*a*, *b*). Approximately 100 mg of each sample powder were dissolved in HF-HNO_3 at 180°C (in Savillex beakers) and re-dissolved twice in 6 M HCl until clear solutions were obtained. Final sample digests were split into two solution aliquots for further processing for Sr–Nd and Hf isotope analysis, respectively. Strontium and the REE fractions were collected using conventional cation exchange chromatography (AG50W-X8, 200–400 mesh). Neodymium was subsequently isolated from the REE fraction using LN Spec resin (50–100 mesh). Hafnium was isolated in a separate procedure that also uses LN Spec resin. The total procedural blanks are negligible at $<$50 pg Sr, $<$30 pg Nd and $<$10 pg Hf (Bast *et al.* 2015; Tappe *et al.* 2020*a*).

Strontium isotope ratio measurements were performed by thermal ionization mass spectrometry on a Thermo Scientific Triton instrument, whereas the Nd and Hf isotope ratios were measured by plasma ionization with a Thermo Scientific Neptune Plus instrument. Measured $^{87}Sr/^{86}Sr$, $^{143}Nd/^{144}Nd$ and $^{176}Hf/^{177}Hf$ ratios were normalized using an

Table 1. *Major (wt%) and trace (ppm) element compositions, as well as Sr–Nd–Hf isotopic compositions of Mesozoic Group 2 kimberlite dykes (orangeites) that intersect the western Bushveld Complex, central Kaapvaal craton, South Africa*

	Impala											Sibanye *(Marikana)*			
	Orangeite						Evolved orangeite					Evolved orangeite			
Sample ID:	IP20-1	IP20-3	IP20-4	IP20-5	IP20-7	IP20-11	IP20-2	IP20-6	IP20-8	IP20-9	IP20-10	LM-4	LM-5	LM-6B1	LM-6B2
Mining block:	Shaft-20	Shaft-20	Shaft-20	Shaft-20	Shaft-20	Shaft-20	Shaft-20	Shaft-20	Shaft-20	Shaft-20	Shaft-20	Karee-3	Karee-3	Saffy	Saffy
SiO_2	39.0	36.7	41.2	40.2	40.2	38.4	38.6	36.4	32.2	38.2	40.1	40.1	38.6	40.1	38.7
TiO_2	0.91	0.78	1.24	1.08	1.09	0.87	2.93	2.83	3.04	1.63	1.31	1.88	1.93	1.89	1.78
Al_2O_3	4.74	6.22	5.55	4.77	4.64	6.64	4.41	4.55	5.66	5.86	5.46	6.37	6.59	6.48	6.28
$Fe_2O_3^T$	7.64	8.05	9.46	8.56	9.39	7.70	12.3	11.3	11.7	10.2	9.06	10.2	10.1	10.3	10.1
MnO	0.13	0.18	0.16	0.14	0.14	0.16	0.22	0.19	0.18	0.19	0.15	0.18	0.17	0.16	0.17
MgO	26.1	22.6	22.8	25.7	22.9	23.2	16.6	16.5	15.1	18.8	20.2	15.5	14.9	15.8	17.1
CaO	7.47	8.69	7.51	6.24	8.68	7.22	10.9	11.7	13.4	8.33	9.76	11.3	10.9	11.8	10.4
Na_2O	0.05	0.12	0.68	0.49	0.58	0.08	1.65	1.48	1.06	1.27	1.53	1.61	1.23	1.14	1.00
K_2O	4.31	6.19	3.21	3.28	3.15	6.22	5.01	5.23	5.28	6.90	3.29	3.23	4.38	3.15	3.76
P_2O_5	0.35	0.10	0.61	0.48	0.66	b.d.	1.72	1.70	1.18	0.61	0.54	0.91	0.97	0.90	0.89
Cr_2O_3	0.38	0.31	0.22	0.22	0.22	0.29	0.15	0.13	0.15	0.23	0.20	0.16	0.16	0.16	0.17
NiO	0.14	0.10	0.13	0.15	0.14	0.11	0.07	0.07	0.05	0.08	0.11	0.06	0.05	0.06	0.06
LOI	6.9	8.3	5.3	6.7	5.8	7.0	3.0	4.8	7.7	5.3	5.8	6.3	7.5	6.0	8.3
Total	98.0	98.4	98.0	97.9	97.7	97.9	97.6	96.8	96.8	97.5	97.5	97.8	97.4	97.9	98.7
CO_2	2.0	4.7	0.28	1.6	0.45	2.1	0.60	0.33	3.1	0.25	0.40	1.1	3.0	0.63	3.0
SO_3	0.19	0.35	0.51	0.65	1.2	b.d.	0.38	0.44	0.76	0.10	1.0	0.29	0.12	0.32	0.21
Co	56.1	53.8	55.1	57.3	56.4	70.4	51.5	48.5	47.3	59.6	65.0	58.3	54.8	58.5	59.7
Cr	811	1503	454	419	465	1694	701	558	415	1260	485	496	529	460	563
Ni	871	655	807	930	850	776	441	432	302	579	798	430	341	427	454
Cu	38.8	5.9	37.5	29.2	37.1	8.5	96.5	94.6	39.6	52.9	49.1	63.5	63.2	63.3	59.7
Zn	37.1	34.4	51.6	40.6	51.9	47.6	66.4	65.3	59.6	76.4	74.6	82.8	85.8	88.5	82.0
Sc	8.6	7.4	11.5	10.2	11.3	19.6	24.8	25.8	21.3	15.6	18.6	23.1	23.2	22.9	21.1
V	112	17.0	123	96.4	115	27.9	51.3	59.9	110	115	292	215	287	144	286
Ga	6.5	6.7	6.9	6.5	6.6	11.6	10.0	10.2	10.4	15.0	11.9	15.9	16.3	17.0	15.9
Ba	1802	2946	2786	2115	3036	2734	4047	4938	4651	4647	6106	1864	2938	3327	3154
Li	1.62	1.98	5.18	4.39	4.14	4.00	8.08	7.55	5.88	9.69	5.55	10.5	11.0	7.45	10.4
Cs	1.95	2.24	1.35	1.18	1.41	2.72	2.88	2.77	2.49	3.66	2.00	1.91	2.06	1.54	1.84
Rb	153	145	106	91.8	93.3	266	179	173	191	340	153	194	230	172	202
Sr	435	808	720	448	668	797	1061	1189	1417	1047	957	858	942	746	858
Zr	84.2	66.3	110	106	130	68.3	389	397	174	189	149	310	306	307	272
Hf	2.53	2.45	3.88	3.61	4.16	2.57	12.2	13.0	5.84	4.81	4.21	7.80	7.70	7.42	6.67
Nb	50.9	42.2	61.3	48.4	61.4	46.7	120	109	102	60.6	82.9	108	103	107	94.0

Ta	3.07	2.42	3.88	3.14	3.90	4.17	5.81	5.96	5.72	2.43	4.30	4.97	4.89	4.93	4.48
Y	4.51	11.4	9.59	6.19	10.4	12.1	33.9	34.9	19.6	20.4	14.1	21.0	21.2	20.7	19.2
Pb	8.84	4.01	14.0	7.11	13.9	2.74	17.7	19.6	25.2	14.8	41.9	28.3	24.6	27.7	23.4
Th	5.53	8.40	8.71	5.25	9.47	12.9	20.7	25.2	20.2	9.56	13.2	15.9	15.7	15.4	14.2
U	1.76	0.97	1.58	1.77	2.45	1.50	5.91	6.28	5.59	4.85	4.08	4.93	4.40	4.78	4.16
W	5.3	0.25	0.30	0.57	1.5	0.12	0.55	0.65	0.54	0.80	2.5	0.30	1.3	0.20	0.33
La	45.8	55.2	65.7	46.5	67.9	61.2	172.2	199.0	169.0	80.5	83.9	108.3	107.0	102.3	95.9
Ce	91.6	114.5	130.9	92.3	134.6	134.1	344.6	395.8	330.2	147.5	159.5	225.7	212.5	214.2	190.5
Pr	10.63	13.35	15.31	10.90	15.85	15.95	39.57	44.79	36.39	16.82	18.08	24.70	24.94	23.40	22.46
Nd	38.9	47.5	55.4	40.8	57.4	58.9	141.4	157.9	122.2	61.1	65.1	85.1	92.0	79.2	80.1
Sm	6.20	8.38	8.98	6.57	9.65	9.17	25.11	28.30	20.42	11.54	12.38	13.20	14.10	13.36	12.89
Eu	1.66	2.42	2.47	1.77	2.64	2.55	6.53	7.40	5.32	3.72	4.01	3.17	3.63	3.51	3.34
Gd	3.95	5.66	6.30	4.52	6.64	6.34	18.61	20.65	14.42	7.67	7.39	9.96	10.23	9.54	9.28
Tb	0.43	0.73	0.73	0.52	0.80	0.73	2.42	2.67	1.69	0.99	0.84	1.19	1.22	1.14	1.12
Dy	1.48	3.23	2.85	1.99	3.11	2.77	10.44	11.28	6.50	4.35	3.15	4.79	4.83	4.54	4.30
Ho	0.20	0.51	0.43	0.30	0.49	0.40	1.59	1.73	0.96	0.69	0.47	0.70	0.73	0.67	0.64
Er	0.51	1.14	1.01	0.71	1.18	1.10	3.44	3.67	2.26	1.58	1.20	1.76	1.79	1.73	1.57
Tm	0.06	0.17	0.14	0.09	0.16	0.14	0.46	0.49	0.28	0.20	0.15	0.22	0.21	0.22	0.20
Yb	0.35	1.05	0.83	0.58	0.95	0.91	2.54	2.77	1.69	1.10	0.94	1.30	1.31	1.25	1.17
Lu	0.05	0.15	0.12	0.09	0.13	0.13	0.34	0.36	0.24	0.15	0.14	0.19	0.19	0.18	0.17
$^{87}Sr/^{86}Sr$ (m)	0.709390(6)	0.708025(7)					0.707962(6)					0.708486(5)	0.708555(7)	0.708592(7)	0.708620(7)
$*^{87}Sr/^{86}Sr$ (i)	0.707410	0.707013					0.707012					0.707218	0.707183	0.707299	0.707293
$^{143}Nd/^{144}Nd$ (m)	0.512243(6)	0.512054(8)					0.512030(6)					0.511993(6)	0.511997(5)	0.512003(7)	0.512010(5)
$*^{143}Nd/^{144}Nd$ (i)	0.512154	0.511956					0.511932					0.511907	0.511912	0.511909	0.511921
$^{\dagger}\varepsilon$Nd (i)	−5.8	−9.6					−10.1					−10.6	−10.5	−10.6	−10.3
2 SD	0.44	0.42					0.41					0.44	0.44	0.43	0.43
$^{176}Hf/^{177}Hf$ (m)	0.282633(7)	0.282476(7)					0.282301(6)					0.282358(7)	0.282350(6)	0.282352(9)	0.282350(7)
$*^{176}Hf/^{177}Hf$ (i)	0.282626	0.282454					0.282291					0.282349	0.282342	0.282343	0.282340
$^{\ddagger}\varepsilon$Hf (i)	−2.5	−8.6					−14.4					−12.3	−12.6	−12.5	−12.6
2 SD	0.73	0.65					0.70					0.72	0.71	0.75	0.72
$\Delta\varepsilon$Hf (i)	5.4	5.5					0.4					3.3	2.8	3.0	2.5

Major and minor element concentrations are X-ray fluorescence spectrometry data determined at the University of Johannesburg; b.d., below detection.
Trace element concentrations are solution ICP–MS data determined at the University of the Witwatersrand. The CO_2 concentrations were determined at the University of Münster.
$Fe_2O_3^T$ = total Fe as ferric iron; LOI, loss on ignition, is defined as the difference in sample weight after ignition at 930°C for 30 min.
Sr isotope ratios were determined by thermal ionization mass spectrometry, and Nd–Hf isotope ratios were determined by MC–ICP–MS at the University of Münster.
*Initial isotope ratios calculated for a magma emplacement age of 140 Ma (Tappe *et al.* 2018) using the following decay constants: ^{87}Rb 1.42×10^{-11}, ^{147}Sm 6.54×10^{-12} and ^{176}Lu 1.865×10^{-11} per year.
†Initial εNd values calculated using ^{147}Sm decay constant of 6.54×10^{-12} per year (Lugmair and Marti 1978); $(^{143}Nd/^{144}Nd)_{CHUR} = 0.512630$ and $(^{147}Sm/^{144}Nd)_{CHUR} = 0.1960$ (Bouvier *et al.* 2008).
‡Initial εHf values calculated using ^{176}Lu decay constant of 1.865×10^{-11} per year (Scherer *et al.* 2001); $(^{176}Hf/^{177}Hf)_{CHUR} = 0.282785$ and $(^{176}Lu/^{177}Hf)_{CHUR} = 0.0336$ (Bouvier *et al.* 2008). CHUR, Chondritic uniform reservoir.
The 2 SD uncertainties of the εNd and εHf values entail a full error propagation, where the uncertainties of the emplacement age and parent–daughter element ratios were set at 20 and 5%, respectively.
$\Delta\varepsilon$Hf (i) is defined as $\varepsilon_{Hf}^{i} - (1.59 \times \varepsilon_{Nd}^{i} + 1.28)$, such that analyses with positive values fall by definition above the Nd–Hf isotope regression line of Chauvel *et al.* (2008).
Numbers in parentheses are 2-sigma-of-the-mean uncertainties for individual isotope ratio measurements.

exponential mass fractionation law and $^{88}Sr/^{86}Sr$ of 8.37521, $^{146}Nd/^{144}Nd$ of 0.7219 and $^{179}Hf/^{177}Hf$ of 0.7325, respectively. The measured Sr–Nd–Hf isotope ratios for all 'unknowns' including the secondary standards are reported relative to $^{87}Sr/^{86}Sr$ of 0.710245 for NBS987, $^{143}Nd/^{144}Nd$ of 0.512115 for JNdi-1 and $^{176}Hf/^{177}Hf$ of 0.282160 for AMES/ JMC-475 standard solutions, respectively. During the analyses in 2020, repeated measurements of $^{87}Sr/^{86}Sr$ for the NBS987 primary standard averaged 0.710282 ± 21 (2 SD, $n = 4$), $^{143}Nd/^{144}Nd$ for the JNdi-1 primary standard averaged 0.512069 ± 8 (2 SD, $n = 12$) and $^{176}Hf/^{177}Hf$ for the AMES primary standard averaged 0.282137 ± 17 (2 SD, $n = 14$).

We also processed the USGS basaltic reference materials BCR-2 and BHVO-2 alongside our samples, and the results are in excellent agreement with the recommended isotope ratios. For BCR-2 the measured values are: $^{87}Sr/^{86}Sr = 0.704996 \pm 6$; $^{143}Nd/^{144}Nd = 0.512634 \pm 25$; and $^{176}Hf/^{177}Hf = 0.282869 \pm 17$. For BHVO-2 the measured values are: $^{87}Sr/^{86}Sr = 0.703471 \pm 6$; $^{143}Nd/^{144}Nd = 0.512990 \pm 9$; and $^{176}Hf/^{177}Hf = 0.283100 \pm 37$. We also processed and analysed the Mintek kimberlite reference material SARM-39 during this analytical session in 2020, and the measured values are: $^{87}Sr/^{86}Sr = 0.708849 \pm 7$; $^{143}Nd/^{144}Nd = 0.512610 \pm 7$; and $^{176}Hf/^{177}Hf = 0.282595 \pm 63$. The results for this matrix-matched reference material are in excellent agreement with the recommended Sr–Nd–Hf isotope ratios for SARM-39 (Tappe *et al.* 2020*a*).

For our samples, the parent–daughter element ratios were calculated using the Rb, Sr, Sm, Nd, Lu and Hf concentrations determined by solution-mode ICP-MS analysis. The initial isotope ratios and notations are calculated at 140 Ma (Tappe *et al.* 2018) and the 2 SD uncertainties of the calculated initial epsilon Nd and Hf values reported in Table 1 entail a full propagation of 'errors'. The error propagation comprises highly conservative uncertainty estimates, i.e. 20% for the *c.* 140 Ma magma emplacement age (140 ± 30 Ma) and 5% for the parent–daughter element ratios. The age corrections are based on the following decay constants: ^{87}Rb 1.42×10^{-11}, ^{147}Sm 6.54×10^{-12} and ^{176}Lu 1.865×10^{-11} per year.

Results

For convenience, results are described separately for the samples from the Impala and Sibanye mining concessions, despite the fact that they are derived from a single large potassic ultramafic dyke swarm. All data generated during this study (i.e. mineral and bulk rock compositions including Sr–Nd–Hf isotope ratios) are provided online in Supplementary Material 1. In addition, the complete bulk rock geochemical dataset is reported as Table 1 in the main article.

Petrography and classification

Our mineralogy and geochemistry data (see below) reveal that the highly micaceous ultramafic dykes intersecting the western Bushveld Complex represent 'typical' Kaapvaal orangeites (formerly Group 2 kimberlites), in contrast to their previous categorization as lamprophyres (cf. Hughes *et al.* 2016). A lamprophyric character can also be excluded on the basis of petrography (Fig. 3), with the absence or paucity of hydrous mafic phenocrysts/macrocrysts and phlogopite being largely confined to the groundmass (Rock 1991; Tappe *et al.* 2005). On a macroscopic scale, the orangeite dykes studied comprise olivine-rich and olivine-poor varieties; the latter are, hereafter, designated as 'evolved' orangeites (Fig. 2c).

The Impala orangeite samples have inequigranular textures with fairly abundant olivine macrocrysts (up to 15 vol%), ranging in size from 1 to 10 mm, as well as highly abundant microphenocrysts (100–500 μm) of phlogopite laths and clinopyroxene prisms (Fig. 3). These coarse to fine crystal populations are set in a very fine-grained groundmass (<100 μm) dominated by phlogopite and clinopyroxene with minor amounts of spinel-group minerals, apatite, carbonate and serpentine (Fig. 3). The olivine macrocrysts are largely serpentinized but rare relict olivine cores have been observed and analysed (see below). The phlogopite laths are typically zoned displaying pale yellow cores and deep orange rims under plane polarized light (Fig. 3a). Rare serpentinized peridotitic microxenoliths up to 20 mm across also occur.

The more evolved orangeite dykes from the Impala and Sibanye mining concessions mostly lack inequigranular textures because olivine macrocrysts are very rare or even absent (<2 vol%; Fig. 2c). However, the common occurrence of aggregates of phlogopite laths >500 μm in length results in a micro-glomeroporphyritic texture. Locally, phlogopite laths show preferred orientations as part of prominent flow structures (Fig. 3c). Rare olivine microcrysts displaying core–rim zoning are observed as inclusions within larger complexly zoned phlogopite plates (Fig. 3f). The phlogopite–diopside dominated groundmass of the evolved orangeites is petrographically similar to its counterpart in the more primitive orangeite dykes, but in addition it may contain subordinate amounts of K-feldspar (?sanidine) and andradite-rich magmatic garnet. Groundmass phlogopite in the evolved orangeite dykes studied may show a decussate texture with randomly oriented and interlocking laths (Fig. 3d–f).

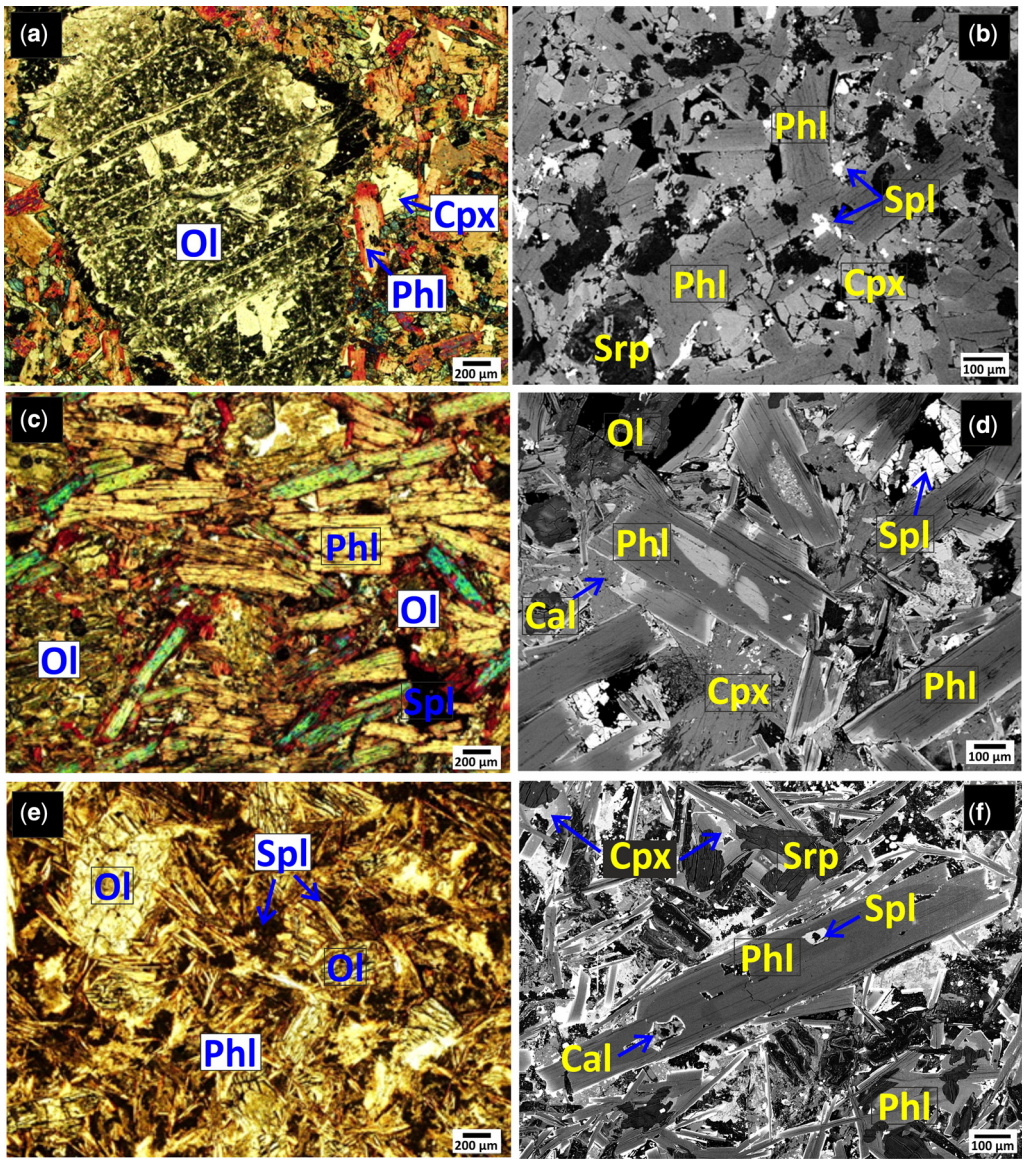

Fig. 3. Photomicrographs and BSE images of representative samples from Bushveld-intersecting orangeite dykes. (**a**) Impala orangeite dyke IP20-1 exhibiting a serpentinized olivine macrocryst set in a phlogopite–clinopyroxene dominated groundmass (plane polarized light). (**b**) Impala orangeite dyke IP20-1 exhibiting abundant zoned phlogopite laths in the groundmass plus interstitial clinopyroxene, Cr-rich spinel and serpentine (?pseudomorphic after olivine microphenocrysts). (**c**) Impala evolved orangeite dyke IP20-9 exhibiting flow-aligned phlogopite laths that drape around serpentinized olivine microphenocrysts. Note the discrete groundmass Cr-rich spinel grains (cross polarized light). (**d**) Impala evolved orangeite dyke IP20-2 exhibiting complexly zoned phlogopite laths and plates in the groundmass plus interstitial acicular clinopyroxene prisms, equant Cr-rich spinel grains and calcite. Note also the serpentinized subhedral olivine microphenocryst. (**e**) Sibanye evolved orangeite dyke LM4 characterized by rare serpentinized subhedral olivine microphenocrysts set in a fine groundmass that is dominated by acicular phlogopite and clinopyroxene plus rare equant Cr-rich spinel grains (plane polarized light). (**f**) Sibanye evolved orangeite dyke LM5 showing a zoned and inclusion-bearing phlogopite microphenocryst set in a fine groundmass that is dominated by acicular phlogopite and clinopyroxene laths forming a decussate micro-texture. Cal, Calcite; Cpx, clinopyroxene; Ol, olivine; Phl, phlogopite; Spl, spinel; Srp, serpentine.

Mineral compositions

Olivine. Owing to widespread alteration of olivine to serpentine (Fig. 3a), olivine major and minor element analysis was only possible for orangeite dyke samples from the Impala mining concession (Supplementary Material 1). Olivine in the Impala orangeite dykes shows a rather restricted compositional range with high forsterite (91.9–93.6 mol%) and NiO (0.33–0.42 wt%) contents at <0.07 wt% CaO (Fig. 4). These compositions resemble those of peridotite-derived mantle xenocrysts reported from kimberlites and related rocks on cratons worldwide (Kamenetsky *et al.* 2008; Tappe *et al.* 2009; Bussweiler *et al.* 2015; Howarth and Taylor 2016; Giuliani 2018; Shaikh *et al.* 2019; Rooney *et al.* 2020; Ngwenya and Tappe 2021). Olivine in the evolved orangeite dykes has slightly lower forsterite contents (90.8–92.4 mol%) at elevated NiO (0.38–0.46 wt%), CaO (0.11–0.

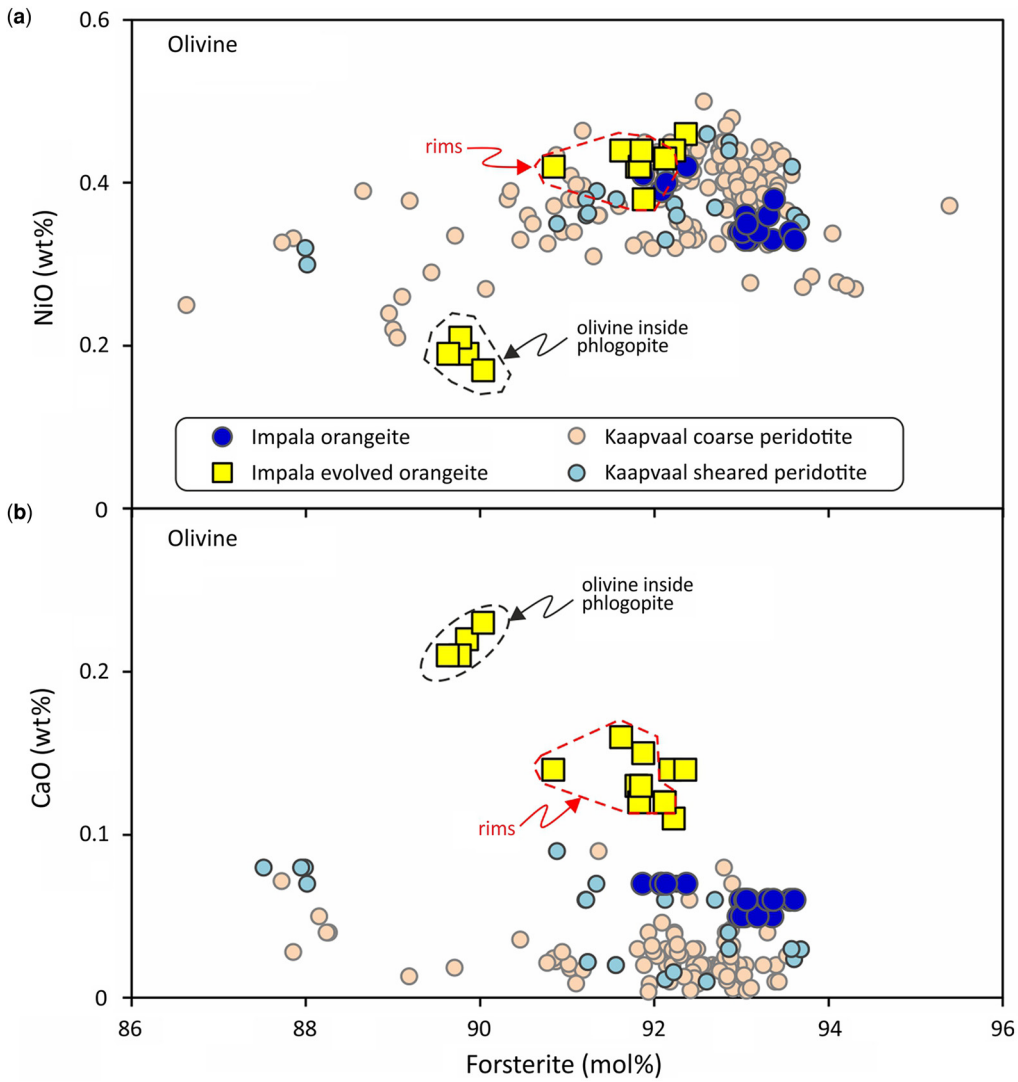

Fig. 4. Olivine major and minor element compositions in Bushveld-intersecting orangeite and evolved orangeite dykes from Impala. (**a**) NiO v. forsterite contents. (**b**) CaO v. forsterite contents. Published olivine compositions for coarse and sheared peridotite xenoliths from the Kaapvaal craton are shown for comparison and the data are listed in Supplementary Material 1 together with the literature sources.

16 wt%) and MnO (0.11–0.16 wt%) concentrations (Fig. 4), which is more typical of magmatic olivine in ultrapotassic systems such as lamproites (Prelevic and Foley 2007; Jaques and Foley 2018; Howarth and Giuliani 2020). Olivine inclusions in phlogopite have the lowest forsterite (89.6–90.0 mol%) and NiO (0.17–0.21 wt%) contents at elevated CaO (0.21–0.23 wt%) and MnO (0.20–0.22 wt%) (Fig. 4), suggestive of a magmatic origin during the early stages of groundmass crystallization.

Phlogopite. Phlogopite is the dominant mica type in the Impala and Sibanye orangeite dykes, where it is largely restricted to the groundmass (Fig. 3). However, phlogopite microphenocrysts also occur in the form of laths and plates ranging in size between 0.3 and 1 mm. They show complex zoning and typically contain minute inclusions of spinel, olivine and carbonate (Fig. 3f). The phlogopite laths and plates are commonly intersected by prismatic groundmass diopside establishing their somewhat earlier crystallization during fast cooling of the narrow dykes (Fig. 3d).

Phlogopite laths and plates in both the olivine-rich and olivine-poor (*or* evolved) orangeite dykes from Impala have similar core compositions that are MgO-rich and relatively poor in Al_2O_3 and FeO, similar to the phlogopite core compositions in the evolved orangeites from Sibanye (Fig. 5a–c). Although phlogopite from the three sample subsets has evolved by Al-depletion and Fe-enrichment (i.e. a tetraferriphlogopite trend), we note subtle differences in the individual core–rim trends relating to the magnitude of the Al–Fe fractionation (Fig. 5a, b). Moreover, phlogopite from the olivine-rich Impala orangeites shows strong Ti-depletion towards the rims, whereas micas in the evolved orangeites from Impala and Sibanye have constant or increasing TiO_2 concentration levels, respectively, towards the rims (up to 4.8 wt% TiO_2; Fig. 5a). In general, the Al–Ti–Fe systematics of phlogopite in the potassic ultramafic dykes from the western Bushveld Complex are typical for Kaapvaal craton orangeites (Mitchell 1995), and only the most evolved dyke compositions from the Sibanye mining concession show a subtle lamproitic mica affinity (e.g. Ti-enrichment). An affinity of the Impala and Sibanye dykes to ultramafic lamprophyres can be largely ruled out because of their generally low Al_2O_3 contents of mica ($\ll$13.5 wt%), which is in contrast to the relatively Al-rich phlogopite compositions ($>$14 wt% Al_2O_3) of aillikites from localities worldwide (Tappe *et al.* 2004; Tappe *et al.* 2006; Nielsen *et al.* 2009; Nasir *et al.* 2011; Dalton *et al.* 2019; Fig. 5a).

The Cr_2O_3 contents of phlogopite in the orangeite dykes from the western Bushveld Complex are mostly $<$1 wt%. However, rare resorbed mica cores in the olivine-rich Impala dykes and more evolved Sibanye dykes reach higher Cr_2O_3 concentration levels of up to 1.8 wt% (Fig. 5c). The phlogopite BaO and F concentration levels are typically below 1 wt%, which presents a marked compositional difference to archetypal kimberlites (Giuliani *et al.* 2016) and cratonic lamproites (Ngwenya and Tappe 2021). These Ba–F systematics are similar to those of phlogopite in ultramafic lamprophyres such as type aillikite (Tappe *et al.* 2006). Very rare biotite laths occur only in the evolved orangeite dykes from the Impala and Sibanye mining concessions, and they show some of the highest Al_2O_3 (up to 14.3 wt%) and F (up to 1.1 wt%) contents among the analysed micas at very low Mg# ($<$45) and Cr_2O_3 ($<$0.1 wt%) (Fig. 5c).

Clinopyroxene. Clinopyroxene is diopside-rich and occurs as small prismatic microphenocrysts (coeval with the phlogopite microphenocrysts) and needle-shaped crystals in the groundmass of the orangeite dykes that intrude the western Bushveld Complex. It also occupies interstitial space between slightly larger interlocking phlogopite laths (Fig. 3b, d). Although subtle compositional zoning has been observed for the clinopyroxene prisms, it is not as prominent as for the coexisting phlogopite laths and plates.

Clinopyroxene in the Impala orangeite dykes has an almost pure diopside composition ($En_{44.3–49.6}Wo_{50.3–51.6}Fs_{0–5.3}$) with very low Al_2O_3 ($<$0.5 wt%) and TiO_2 ($<$1 wt%) contents (Fig. 5d). Diopside-rich clinopyroxene in the groundmass of the evolved orangeite dykes from both the Impala and Sibanye mining concessions ($En_{40.0–49.1}Wo_{49.7–51.6}Fs_{0–10}$) is also Al_2O_3 poor ($<$0.5 wt%), but it has notably higher TiO_2 concentrations compared with diopside in the more primitive olivine-rich dykes from Impala, ranging between 1.6 and 2.6 wt% (Fig. 5d). The Cr_2O_3 and Na_2O contents of clinopyroxene are similarly low for the three sample subsets, reaching up to 0.2 and 1.36 wt%, respectively. These groundmass clinopyroxene compositions are typical for Kaapvaal craton orangeites (Mitchell 1995), whereas they differ greatly from the much more Al- and Ti-enriched groundmass diopside compositions of ultramafic lamprophyres from localities worldwide (e.g. Tappe *et al.* 2004, 2006; Dalton *et al.* 2019; Fig. 5d).

Spinel-group minerals. Spinel-group minerals are common accessory constituents of the petrographically diverse samples from the orangeite dyke swarm examined here. They typically occur as $<$50 μm euhedral to subhedral inclusions within microphenocrystic olivine and phlogopite, but are only rarely observed as $<$100 μm groundmass phase occupying textural interstices (Fig. 3). Atoll-

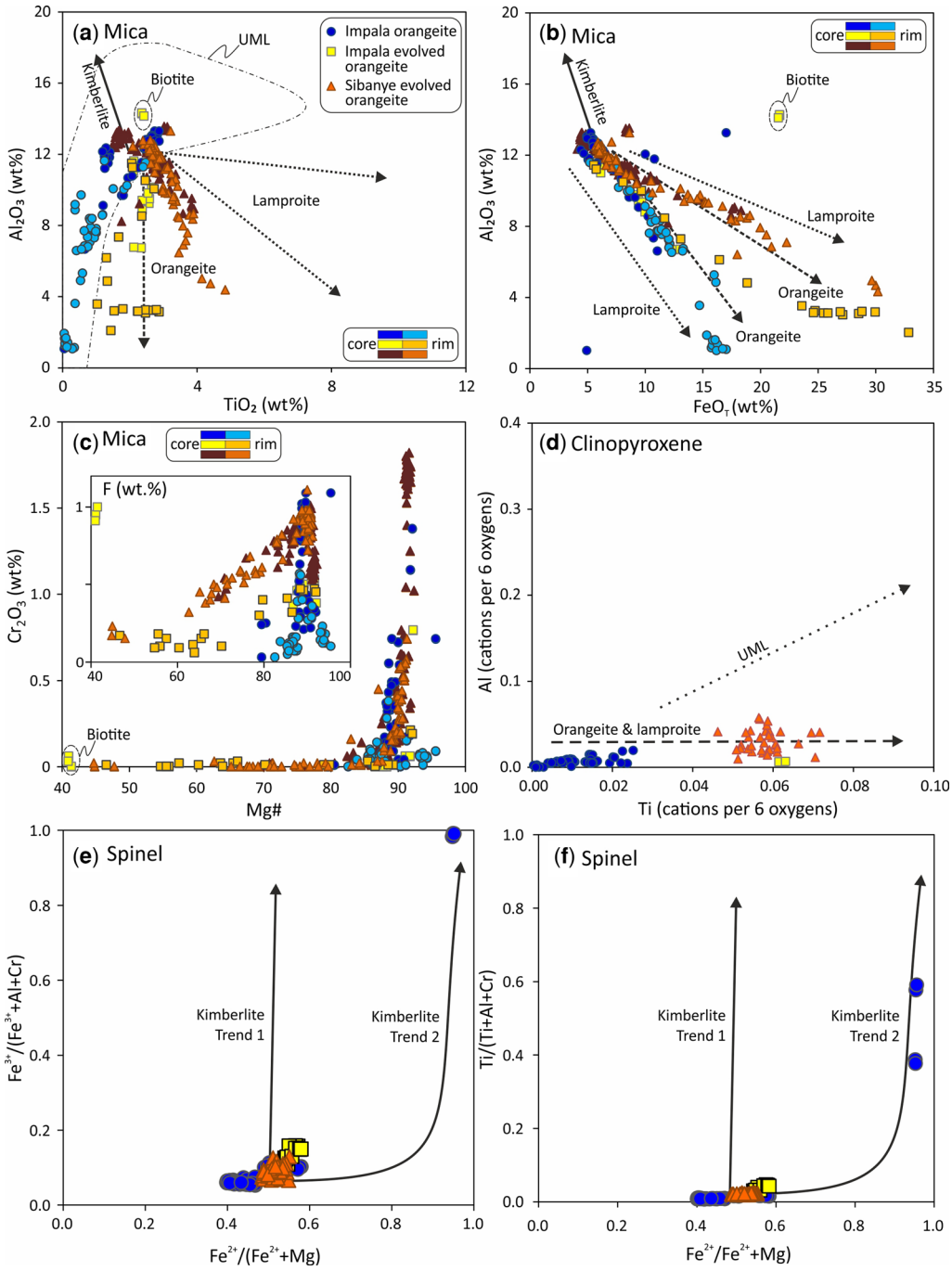

Fig. 5. Major and minor element compositions of petrogenetically important mineral constituents of Bushveld-intersecting orangeite dykes. (**a**) Al_2O_3 v. TiO_2; (**b**) Al_2O_3 v. total FeO; and (**c**) Cr_2O_3 and F v. Mg-number for abundant phlogopite and rare biotite in the groundmass. (**d**) Atomic Al v. Ti contents of diopside-rich groundmass clinopyroxene. (**e**) $Fe^{3+}/(Fe^{3+} + Al + Cr)$ and (**f**) $Ti/(Ti + Al + Cr)$ v. $Fe^{2+}/(Fe^{2+} + Mg)$ for groundmass spinel. Mineral compositional trends that are typical for kimberlites, lamproites and orangeites are taken from Mitchell (1995), whereas those for ultramafic lamprophyres *or* UML are adopted from Tappe *et al.* (2004, 2005, 2006).

textures, as commonly observed for groundmass spinel in archetypal kimberlite and aillikite (Mitchell 1986; Tappe *et al.* 2006), are notably absent in our orangeite samples. Spinel in the Impala orangeite dykes evolved from chromite to Ti-rich magnetite along a trajectory reminiscent of 'Kimberlite Trend 2', although intermediate compositions are conspicuously absent (Fig. 5e, f). Such an evolutionary trend at increasing Fe^{2+}/Mg is typical for Kaapvaal craton orangeites, but also for cratonic lamproites from localities worldwide (Mitchell and Bergman 1991; Mitchell 1995). In contrast, groundmass spinel compositional evolution in bona fide kimberlite magmatic systems occurs along relatively constant and low Fe^{2+}/Mg, the so-called 'Kimberlite Trend 1' (Mitchell 1986; Roeder and Schulze 2008). However, recent work has shown that evolutionary paths in between the two major 'kimberlitic' spinel trends may be followed by both archetypal kimberlites and aillikites (Tappe *et al.* 2009; Tappe *et al.* 2014; Dongre and Tappe 2019). This observation renders spinel compositions less diagnostic for the identification of volatile-rich ultramafic magma types than previously thought. Regardless, the evolved orangeites from the Impala and Sibanye mining concessions apparently contain only Cr-rich spinel grains (87.2–91.6 Cr#) that overlap with the compositions of chromite from the more primitive olivine-rich orangeite dykes at Impala (82.1–90.3 Cr#) (Fig. 5e, f).

Andradite garnet. Andradite-rich garnet occurs as <100 μm large groundmass grains within the evolved orangeite dykes of the Impala mining concession. The magmatic garnet grains exhibit very high CaO (32.0–32.5 wt%), TiO_2 (15.8–18.0 wt%) and FeO (17.5–18.2 wt%) contents at <0.01 wt% Cr_2O_3 (Fig. 6). They represent a solid solution series between the andradite, Ti-andradite and schorlomite garnet endmembers, with only a very small pyrope component. The Ti-rich andradite grains analysed here have similar compositions to the primary magmatic Ti-andradite reported from the groundmass of ultramafic lamprophyres on the North Atlantic craton in eastern Canada and West Greenland (Tappe *et al.* 2004; Tappe *et al.* 2006; Tappe *et al.* 2009), as well as from orangeites on the Dharwar craton in southern India (Dongre *et al.* 2016; Choudhary *et al.* 2020; Fig. 6). They are more Ti-enriched than the relatively pure andradite compositions reported from carbonatite dykes of the Premier kimberlite pipe on the central Kaapvaal craton (Fig. 6), which were interpreted to have a secondary origin (Dongre and Tappe 2019). We note that Hammond and Mitchell (2002) reported an 'unidentified Ca–Ti–Fe–silicate' phase from the Swartruggens orangeite dyke swarm some 60 km west of the Bushveld Complex on the central Kaapvaal craton (Fig. 1), and this phase possibly represents Ti-rich andradite of a primary magmatic origin (Fig. 6). Regardless, it appears as though magmatic Ti-andradite is a relatively common accessory mineral in evolved orangeites and, thus, less diagnostic for ultramafic lamprophyres than previously thought (cf. Tappe *et al.* 2005).

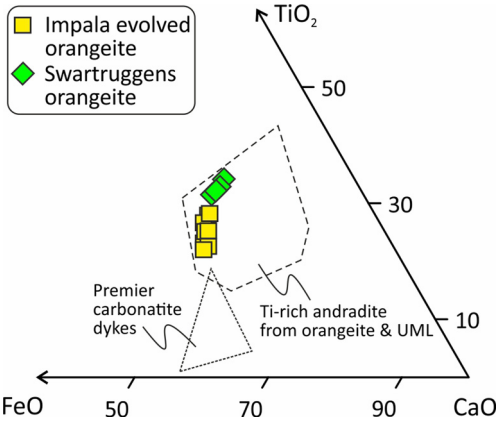

Fig. 6. Andradite garnet CaO–TiO_2–FeO compositions in Bushveld-intersecting evolved orangeite dykes from Impala. Data from a Swartruggens orangeite dyke represent the 'unidentified Ca–Ti–Fe–silicate' phase reported in Hammond and Mitchell (2002), which is interpreted here as magmatic Ti-rich andradite. The field for andradite garnet from carbonatite dykes of the Premier kimberlite pipe on the central Kaapvaal craton is adopted from Dongre and Tappe (2019). The andradite garnet compositional field for ultramafic lamprophyres and orangeites is based on the data reported in Tappe *et al.* (2004, 2006, 2009), Dongre *et al.* (2016) and Choudhary *et al.* (2020).

Bulk rock major and trace element compositions

The Impala orangeite dykes have higher MgO (22.6–26.1 wt%), Cr (419–1694 ppm) and Ni (655–930 ppm) contents than the evolved orangeite dykes from this locality (15.1–20.2 wt% MgO, 415–1260 ppm Cr, 302–798 ppm Ni) and from the Sibanye mining concession (14.9–17.1 wt% MgO, 460–563 ppm Cr, 341–454 ppm Ni). The TiO_2 (0.78–1.24 wt%), CaO (6.24–8.69 wt%), Na_2O (0.05–0.68 wt%) and P_2O_5 (0.10–0.66 wt%) contents are notably lower for the Impala orangeite dykes compared with the evolved varieties from Impala (1.31–3.04 wt% TiO_2, 8.33–13.4 wt% CaO, 1.06–1.65 wt% Na_2O, 0.54–1.72 wt% P_2O_5) and Sibanye (1.78–1.93 wt% TiO_2, 10.4–11.8 wt% CaO, 1.00–1.61 wt% Na_2O, 0.89–0.97 wt% P_2O_5; Fig. 7). The other major and minor elements show

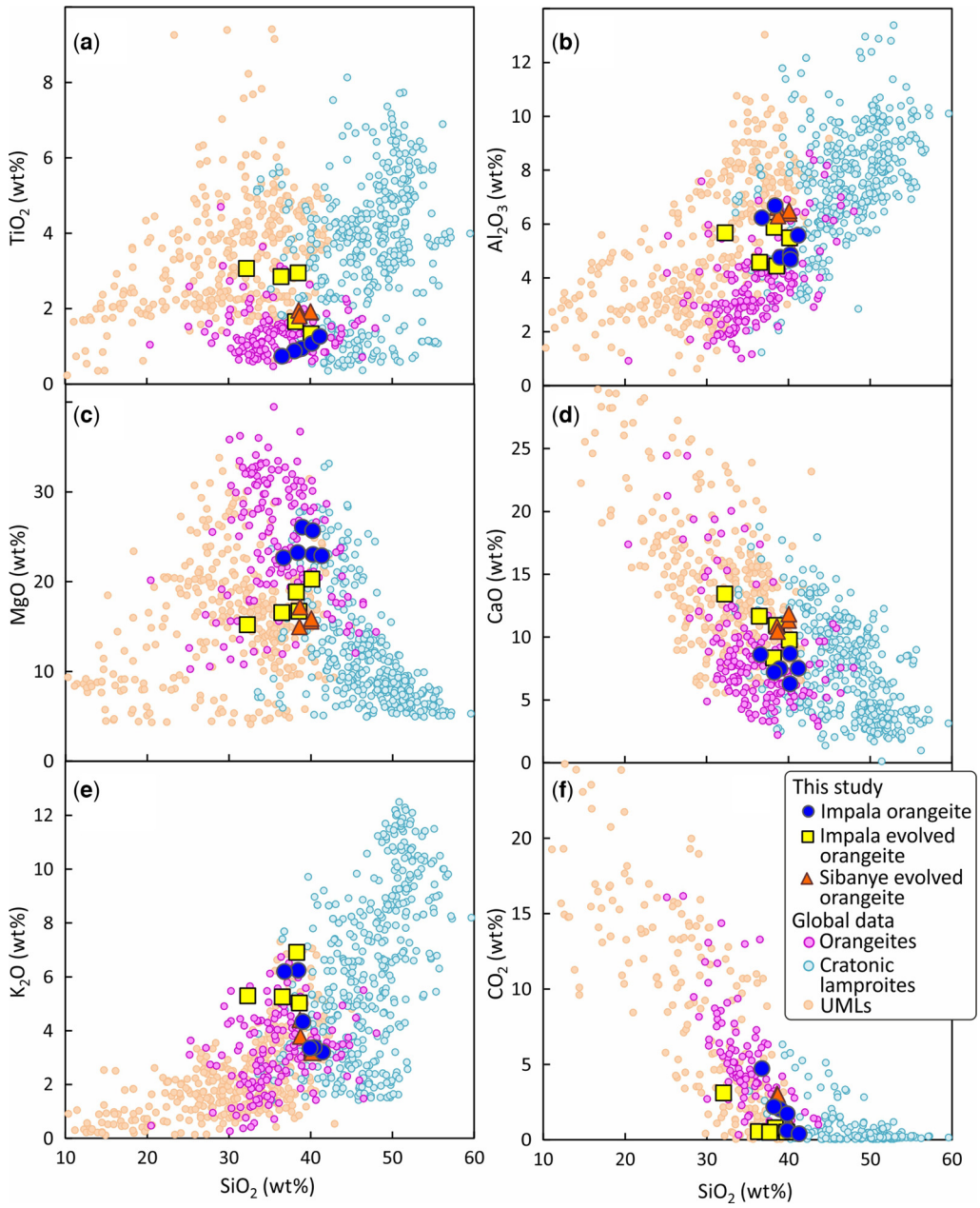

Fig. 7. Bulk rock major element variation diagrams for Bushveld-intersecting orangeite dykes. Data for comparisons with cratonic lamproites and ultramafic lamprophyres from localities worldwide are taken from the compilation of Ngwenya and Tappe (2021), which also contains the summary of data for type orangeites from the Kaapvaal craton as shown here.

broad compositional overlap between the three sample subsets. For example, the SiO_2 (32.2–41.2 wt%), Al_2O_3 (4.41–6.64 wt%) and CO_2 (0.25–4.71 wt%) contents are variably low, whereas the K_2O (3.15–6.90 wt%) concentration levels are collectively high (Fig. 7b, e, f). The entire suite of samples from the Bushveld-intersecting orangeite dyke swarm has a truly 'ultrapotassic' character according to the criteria of Foley *et al.* (1987), with >3 wt% MgO and K_2O, respectively, at $K_2O/Na_2O \geq 2$ (2.0–86.2)

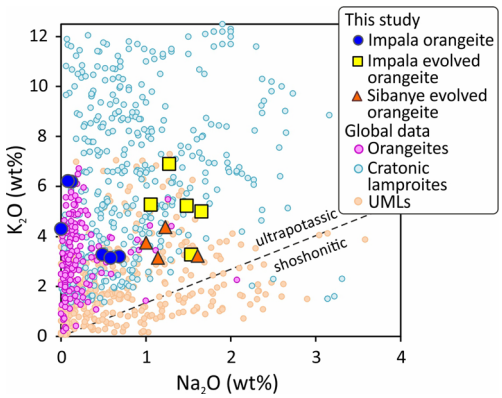

Fig. 8. Bulk rock K_2O–Na_2O variation in Bushveld-intersecting orangeite dykes. Data for comparisons with cratonic lamproites and ultramafic lamprophyres from localities worldwide are taken from the compilation of Ngwenya and Tappe (2021), which also contains the summary of data for type orangeites from the Kaapvaal craton. Note the exclusively ultrapotassic character of Kaapvaal orangeites including the dykes studied here. The ultrapotassic–shoshonitic rock divide is after Peccerillo and Taylor (1976).

(Figs 7 & 8). Compared with other potassic ultramafic rock types, the Bushveld-intersecting ultrapotassic dykes show a good compositional match to typical Kaapvaal craton orangeites (Fig. 7), which is in agreement with their mineral assemblages and compositions (see above). However, there is also some overlap in terms of major element compositions with cratonic lamproites and ultramafic lamprophyres from continental shields worldwide (Figs 7 & 8).

The orangeite dykes analysed here are strongly enriched in incompatible trace elements and they have similar primitive mantle normalized distributions compared with other Kaapvaal craton orangeites (Becker and le Roex 2006; Coe *et al.* 2008) (Fig. 9). Whereas the olivine-rich Impala dykes fall at the lower end of the incompatible element concentration range of Kaapvaal orangeites, the olivine-poor *or* evolved orangeites from the Impala and Sibanye mining concessions cover the middle and upper ranges (Fig. 9), but the trace element patterns for the three sample subsets are very similar (Figs 9 & 10). A characteristic feature of Kaapvaal craton orangeites is their strong LILE (Cs–Rb–Ba–K) enrichment coupled to a marked relative depletion of certain high field strength elements (HFSE; Th–U–Nb–Ta; Coe *et al.* 2008), and the Bushveld-intersecting orangeite dykes studied here are no exception (Fig. 9). This geochemical feature also displays prominently in the Ba/Nb v. La/Nb diagram (Fig. 11a), in which the Impala dykes even extend the level of LILE/HFSE fractionation that is

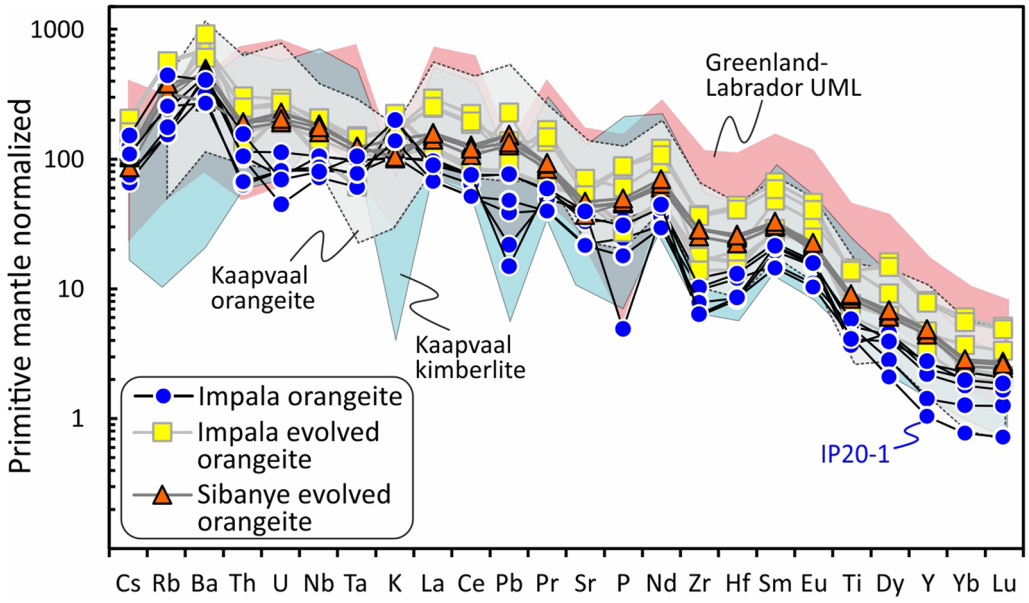

Fig. 9. Normalized incompatible element distributions of Bushveld-intersecting orangeite dykes. Fields for comparisons are based on data from the following literature sources: Kaapvaal kimberlites – le Roex *et al.* (2003), Becker and le Roex (2006), Tappe *et al.* (2020*a*, *b*); Kaapvaal orangeites – Becker and le Roex (2006), Coe *et al.* (2008); Greenland–Labrador UML – Tappe *et al.* (2006, 2008, 2011, 2017), Nielsen *et al.* (2009). The primitive mantle compositional estimate is after Palme and O'Neill (2003). UML, ultramafic lamprophyres.

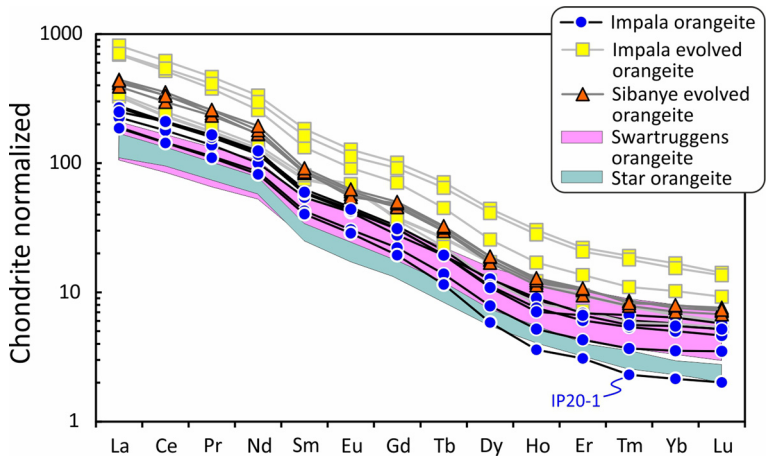

Fig. 10. Normalized rare-earth element (REE) distributions of Bushveld-intersecting orangeite dykes. Fields for the Swartruggens and Star orangeites are based on the data reported in Coe *et al.* (2008). The values for chondrite are after Palme and Jones (2003).

commonly observed for South African orangeites (Becker and le Roex 2006).

Bulk rock Sr–Nd–Hf isotopic compositions

The initial Sr–Nd–Hf isotopic compositions of the Bushveld-intersecting orangeite dykes from the central Kaapvaal craton are calculated for a magma emplacement age of 140 Ma (Table 1; Supplementary Material 1). The initial $^{87}Sr/^{86}Sr$ of the three sample subsets are all elevated and fall within a relatively narrow range between 0.707012 and 0.707410. The range displayed by the corresponding initial $^{143}Nd/^{144}Nd$ is relatively wide, with subchondritic initial εNd values from −10.6 to −5.8, although the majority of samples fall between −10.6 and −9.6 (Fig. 12). The olivine-rich orangeite dykes from Impala tend to have more radiogenic Nd isotopic compositions compared with the olivine-poor *or* evolved orangeite dykes from the Impala and Sibanye mining concessions (Figs 12 & 13). The corresponding initial $^{176}Hf/^{177}Hf$ ratios show even larger variations, with subchondritic initial εHf values from −14.4 to −2.5 (Fig. 13). Similar to the Nd isotope systematics, the olivine-rich orangeite dykes from Impala have more radiogenic Hf isotopic compositions than the evolved varieties. The Bushveld-intersecting orangeite dykes fall firmly within the terrestrial Nd–Hf isotope array (Chauvel *et al.* 2008; Fig. 13), with initial $\Delta\varepsilon$Hf values between +0.4 and +5.5 (Table 1). The positively correlated Nd–Hf isotope systematics are in contrast to the commonly observed isotopic decoupling that characterizes many archetypal kimberlite sample suites from cratons worldwide (for a review see Tappe *et al.* 2020*a*). In general, the combined Sr–Nd–Hf isotope systematics of the Bushveld-intersecting orangeite dykes reveal moderately to strongly enriched source compositions relative to primitive mantle, very similar to those of other orangeite occurrences from across the Kaapvaal craton (Figs 12 & 13).

Discussion

Mesozoic orangeite magmatism on the central Kaapvaal craton

The Swartruggens dyke swarm as a benchmark. The *c.* 145 Ma potassic ultramafic dyke swarm near Swartruggens is one of the best-studied orangeite occurrences on the central Kaapvaal craton and thus provides a benchmark against which to compare the petrogenesis of the Bushveld-intersecting orangeite dykes near Rustenburg (Fig. 1). The Swartruggens dykes, exploited at Helam Diamond Mine, have been variably referred to as kimberlites, lamprophyres, minettes, lamproites and, more recently, as orangeites (Fourie 1958; Skinner and Scott 1979; Mitchell and Bergman 1991; Mitchell 1995; Gurney and Kirkley 1996; Klump and Gurney 1998; Hammond and Mitchell 2002; McKenna *et al.* 2004; Coe *et al.* 2008). Although some studies used this terminology interchangeably, several workers pointed out that the Swartruggens dyke system is structurally and compositionally highly complex, comprising multiple intrusive phases and showing evidence of internal differentiation processes that may have created the highly variable petrographic characteristics and diverse mineralogy

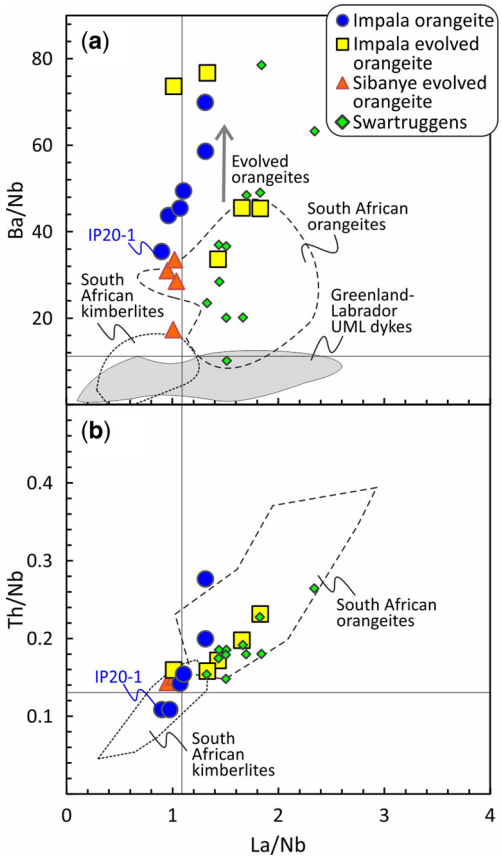

Fig. 11. Incompatible trace element ratios of Bushveld-intersecting orangeite dykes. (**a**) Ba/Nb and (**b**) Th/Nb v. La/Nb. Fields for comparisons are based on data from the following literature sources: South African kimberlites – le Roex *et al.* (2003), Becker and le Roex (2006), Tappe *et al.* (2020*a*, *b*); South African orangeites including the Swartruggens dykes – Becker and le Roex (2006), Coe *et al.* (2008); Greenland–Labrador UML dykes – Tappe *et al.* (2006, 2008, 2011, 2017), Nielsen *et al.* (2009).

(e.g. Skinner and Scott 1979; Mitchell 1995; Gurney and Kirkley 1996). A key observation was that the dykes are unusually poor in or even devoid of olivine macrocrysts. This feature is mirrored by the typically low abundances of mantle-derived indicator minerals such as pyrope garnet and Cr-diopside, compared with much higher indicator mineral counts for diamondiferous orangeites on the western Kaapvaal craton (Field *et al.* 2008). The paucity of mantle-derived indicator minerals stands in contrast to the very high diamond grades in some of the Swartruggens dykes such as the Main Fissure with >200 carats per hundred tonnes of kimberlitic ore. However, diamond-free 'fissures' such as the Muil Dyke occur within a few metres of lateral distance from the highly diamondiferous dykes (Klump and Gurney 1998; McKenna *et al.* 2004). On the basis of a detailed geochemical investigation, Coe *et al.* (2008) concluded that the compositionally highly variable Swartruggens orangeite dykes are related to a common parental magma, which suggests that differentiation processes have a strong control on primitive potassic magma type diversification upon ascent, including redistribution of any possibly existing diamond cargo.

The *c.* 140 Ma orangeite dykes on the western Bushveld Complex studied here are structurally and compositionally very similar to the Swartruggens dyke swarm some 60 km further west (Fig. 1). Our sample suite from these Bushveld-intersecting orangeite dykes allows for an evaluation of the role of crystal fractionation in the evolution of these potassic ultramafic magmas, which is an often-neglected process that operates in the plumbing system of deep-sourced volatile-rich melts on and around cratons worldwide.

Ultrapotassic magma evolution at Impala and Sibanye. The Bushveld-intersecting orangeite dykes comprise relatively olivine-rich and very olivine-poor varieties, illustrated by the example of drillcore intersections in Figure 2c. Importantly, both varieties contain compositionally overlapping Cr–spinel inclusions and discrete groundmass grains (Fig. 5e, f), which suggests a common parental magma to the entire orangeite dyke swarm on the central Kaapvaal craton, similar to the interpretation by Coe *et al.* (2008) for the Swartruggens dyke system.

Although a significant portion of the macrocrystic olivine in the olivine-rich orangeite dykes from Impala is derived from disaggregated cratonic mantle peridotites (i.e. xenocrystic), magmatic olivine is present in these rocks and reveals the diagnostically high Ni and elevated Ca contents commonly observed in olivine that crystallized from ultrapotassic magmas such as lamproites (Prelevic *et al.* 2013; Jaques and Foley 2018). These Ni- and Ca-enriched magmatic olivine compositions partially overlap with those of rare olivine microphenocrysts in the more evolved orangeite dykes. The evolved orangeite dykes contain olivine inclusions in groundmass phlogopite laths and they record magmatic evolution towards lower forsterite and Ni contents at elevated CaO (Fig. 4). Hence, olivine compositions in both the olivine-rich and olivine-poor *or* evolved orangeites provide evidence for magmatic olivine fractionation within this ultrapotassic system, superimposed on the effect of relatively minor xenocrystic olivine addition.

The geochemical variation diagrams in Figure 14, using MgO as a 'differentiation' index, show that the olivine-rich orangeite dykes from Impala have slightly higher MgO contents between 22.6 and

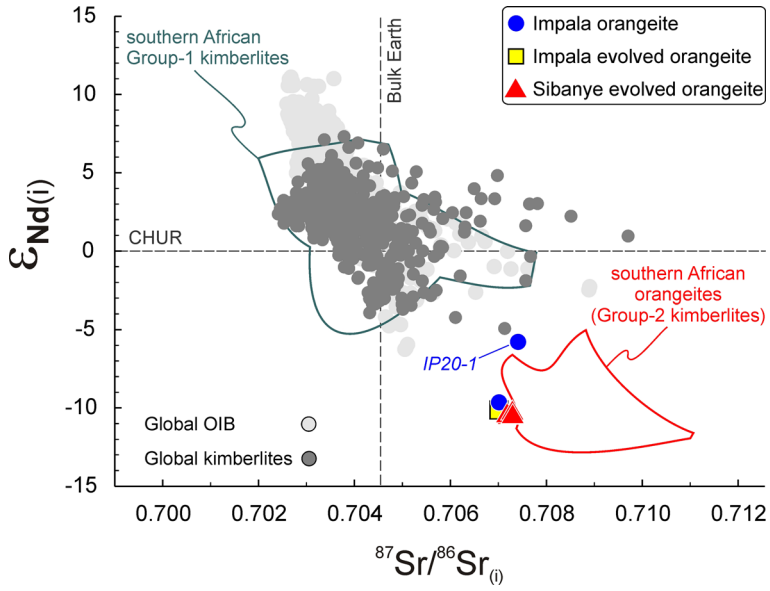

Fig. 12. Initial Sr–Nd isotopic compositions of Bushveld-intersecting orangeite dykes. Analytical uncertainties including a full propagation of errors are smaller than or similar to symbol size (Table 1). Fields for comparisons are based on data from the following literature sources: southern African Group 1 kimberlites – Smith (1983), le Roex *et al.* (2003), Nowell *et al.* (2004), Becker and le Roex (2006), Griffin *et al.* (2014), Sarkar *et al.* (2014), Tappe *et al.* (2020*a*, *b*); southern African Group 2 kimberlites *or* orangeites – Fraser *et al.* (1985), Nowell *et al.* (2004), Becker and le Roex (2006), Coe *et al.* (2008); global kimberlites including groundmass perovskite – Tappe *et al.* (2017); global OIB – Stracke (2012). CHUR, Chondritic uniform reservoir; OIB, oceanic island basalts.

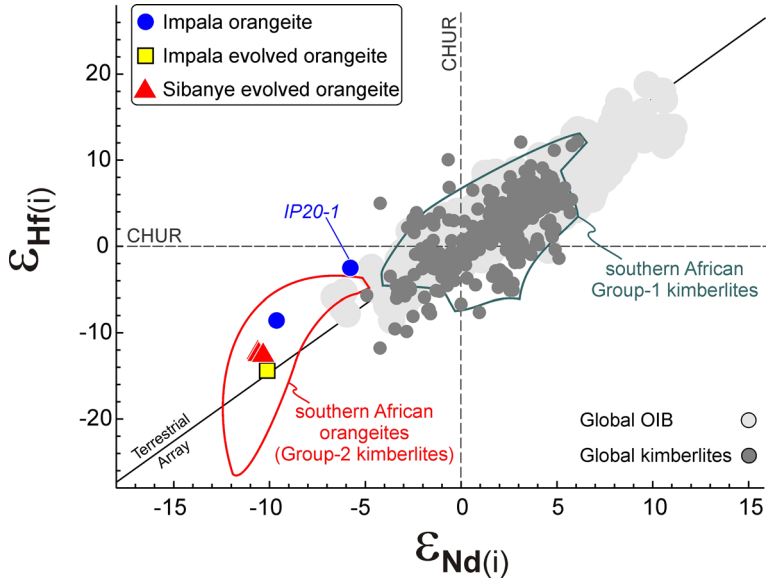

Fig. 13. Initial Nd–Hf isotopic compositions of Bushveld-intersecting orangeite dykes. Analytical uncertainties including a full propagation of errors are smaller than or similar to symbol size (Table 1). Fields for comparisons are based on data from the following literature sources: southern African Group 1 kimberlites – Nowell *et al.* (2004), Tappe *et al.* (2020*a*, *b*); southern African Group 2 kimberlites *or* orangeites – Nowell *et al.* (2004), Coe *et al.* (2008); global kimberlites – Tappe *et al.* (2017); global OIB – Stracke (2012). The terrestrial array regression line is taken from Chauvel *et al.* (2008).

26.1 wt% compared with the estimated close-to-primary magma composition of the Swartruggens orangeite dyke swarm at *c.* 21 wt% MgO (Coe *et al.* 2008). Given the similar age and Sr–Nd–Hf isotopic compositions, plus the close geographic proximity on the central Kaapvaal craton (Fig. 1), it is reasonable to infer that a compositionally similar parental magma supplied both dyke systems. If correct, up to 10% of xenocrystic olivine addition to the parental Impala orangeite magma can explain their higher MgO contents relative to the close-to-primary ultrapotassic magma composition of the Swartruggens dyke swarm (Fig. 14). Regarding the more evolved orangeite varieties from the Bushveld-intersecting dyke swarm, their MgO contents range from 20.2 down to 14.9 wt%, which suggests between 2 and 12% of olivine fractionation, arguably controlled by the removal of magmatic olivine. Alternatively, flowage-segregation and filter-pressing may have contributed to the observed

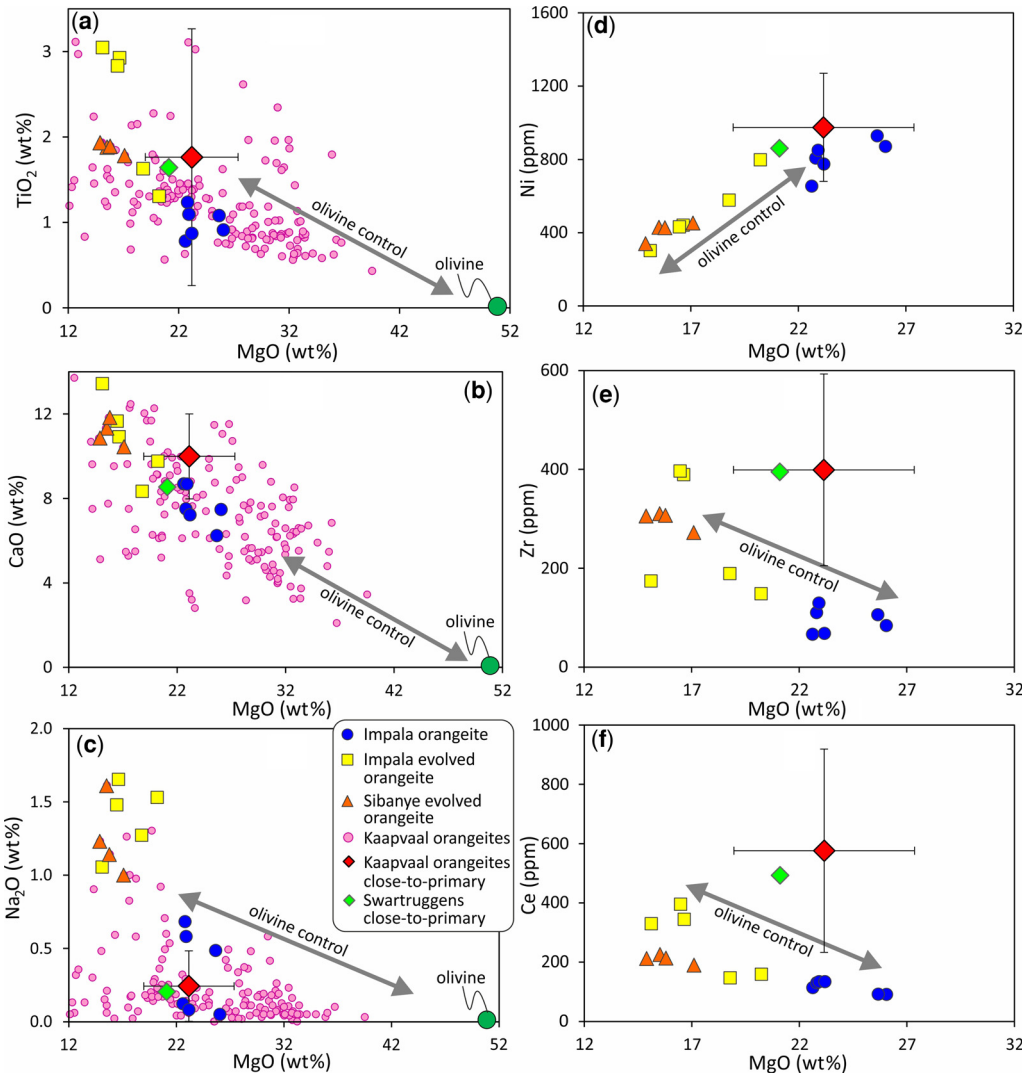

Fig. 14. Bulk rock major (**a–c**) and trace (**d–f**) element variation diagrams for Bushveld-intersecting orangeite dykes using MgO as a differentiation index. The data compilation for type orangeites from the Kaapvaal craton is taken from Ngwenya and Tappe (2021). The estimated close-to-primary magma compositions of Kaapvaal orangeites (error bars at 1-sigma) and Swartruggens orangeites are adopted from Becker and le Roex (2006) and Coe *et al.* (2008), respectively. The inferred olivine control line is guided by olivine compositions from the Impala orangeite dykes (Supplementary Material 1).

geochemical 'olivine control', but such intra-dyke differentiation mechanisms are difficult to quantify in kimberlitic magmatic systems (Kjarsgaard *et al.* 2009; Zurevinski and Mitchell 2011; Tappe *et al.* 2014; Abersteiner *et al.* 2019). Regardless of the circumstances of olivine control, it is generally accepted that olivine and diamond crystals are transported in a similar manner within flowing and erupting kimberlitic magmas, mainly because of their similar densities (Grunsky and Kjarsgaard 2008; Field *et al.* 2009; Moss *et al.* 2010). Thus, identification of olivine fractionation helps to explain the lack of diamonds in the Bushveld-intersecting orangeite dykes on the central Kaapvaal craton, a geological domain that has a highly diamondiferous lithospheric mantle root (Viljoen *et al.* 2004; Field *et al.* 2008; Korolev *et al.* 2018; Tappe *et al.* 2018; Smart *et al.* 2021; Fig. 1).

A firm olivine control on the petrogenetic link between the Impala orangeites and the more evolved varieties from Impala and Sibanye is also supported by both compatible (e.g. Ni) and incompatible (e.g. Zr, Ce) trace element variations with varying MgO contents (Fig. 14d–f). Furthermore, the similar primitive mantle normalized incompatible element patterns of the olivine-rich and olivine-poor orangeite varieties, with a systematic offset to higher trace element abundances in the samples with the lowest modal olivine content, are best explained by olivine fractionation (Fig. 9). This effect is also evident in the chondrite-normalized REE diagram (Fig. 10), where complete compositional overlap exists between the most primitive Swartruggens and Impala orangeite dykes, whereas the more evolved varieties from Impala and Sibanye exhibit up to an order of magnitude higher REE concentrations, at broadly parallel element distributions for all rock suites discussed here (Fig. 10).

K-metasomatized cratonic mantle sources. Similar to global anorogenic lamproite volcanism, type orangeites from the Kaapvaal craton and adjoining mobile belts are characterized by strongly enriched Sr–Nd–Hf isotopic compositions (Nowell *et al.* 2004). The long-term enriched geochemical signature of the mantle source to orangeite magmatism stands in contrast to the more primitive and moderately depleted isotopic compositions of archetypal kimberlites in southern Africa (Figs 12 & 13). The striking isotopic difference between the two major diamond 'delivery' systems on the Kaapvaal craton forms the basis of petrogenetic models that invoke ancient metasomatized lithospheric mantle sources for orangeites as opposed to asthenospheric sources for kimberlites (Smith 1983; Fraser *et al.* 1985; Nowell *et al.* 2004; Tappe *et al.* 2020*a*, *b*).

The Sr–Nd–Hf isotopic compositions of the Bushveld-intersecting orangeite dykes from the central Kaapvaal craton are similar to those of other orangeite localities in South Africa, including the Swartruggens dyke swarm (Coe *et al.* 2008; Figs 12 & 13). For the Impala and Sibanye dykes, the olivine-rich and more evolved orangeite varieties have broadly overlapping isotopic compositions, but we note that dyke IP20-1 shows significantly higher Nd and Hf isotope ratios at similarly radiogenic $^{87}Sr/^{86}Sr$, when compared with the other orangeite dykes (Figs 12 & 13). Dyke IP20-1 from Impala also shows more extreme HREE depletion and, altogether, these geochemical features suggest a more notable interaction of the ultrapotassic melt with much less enriched lithologies within the Kaapvaal cratonic mantle root (Figs 9–13). This material was probably clinopyroxene bearing, because among common cratonic mantle minerals it is the only phase that can significantly influence the Nd and Hf budgets of passing melts alike, retaining isotopic coupling (Griffin *et al.* 2000). Alternatively, the detected variability in the Nd–Hf isotopic compositions of the Bushveld-intersecting orangeite dykes may reflect lithospheric mantle source heterogeneity. For example, MARID-type metasomes have frequently been invoked as source components to potassic ultramafic magmas (Foley 1992; Ulmer and Sweeney 2002; Tappe *et al.* 2008; Smart *et al.* 2019), and isotopic investigations of such heavily K-metasomatized lithospheric mantle materials revealed extreme heterogeneity down to the centimetre scale (Kramers *et al.* 1983; Grégoire *et al.* 2002; Choukroun *et al.* 2005; Fitzpayne *et al.* 2019).

A 'stored' subduction signature in Kaapvaal cratonic mantle metasomes. Type orangeites from South Africa collectively exhibit a strong Cs–Rb–Ba–K enrichment that is coupled to a relative depletion in Th–U–Nb–Ta (Becker and le Roex 2006; Coe *et al.* 2008; this study). This distinctive trace element signature is associated with remarkably low TiO_2 contents of <2 wt% for the most primitive orangeite varieties (Figs 7a & 9), much lower than what is typically observed for other potassic ultramafic magma types on cratons, such as anorogenic lamproites and aillikites, which reach up to 8 wt% TiO_2 (Figs 7a & 9). The high LILE/HFSE ratios of Kaapvaal craton orangeites are reminiscent of a classic subduction zone signature (Fig. 11), where residual titanate minerals (e.g. rutile) in the downgoing oceanic slab retain in particular Ti–Nb–Ta while the LILE (and LREE) become enriched in extracted melts/fluids and enter the lithospheric mantle of the overriding tectonic plate (Foley and Wheller 1990; Pearce and Peate 1995).

As Coe *et al.* (2008) pointed out, the Kaapvaal craton was last subjected to subduction and collisional events in its immediate vicinity during the Mesoproterozoic Namaqua–Natal orogeny at

1220–1090 Ma (Spencer *et al.* 2015). Although the geometry of these ancient subduction zones is far from understood (Jacobs *et al.* 2008; Van Schijndel *et al.* 2020), it is reasonable to assume that oceanic slab remnants temporarily stalled beneath the thick Kaapvaal lithosphere and released small volumes of metasomatic melts/fluids by which the widespread 'subduction' signature was introduced into the lowermost cratonic mantle. Structural responses of the Kaapvaal lithosphere to these Mesoproterozoic collisions are evident from its burial and unroofing history (Baughman and Flowers 2020), and also from the prolonged emplacement history of the Premier kimberlite cluster in the central part of the craton between *c.* 1155 and 1135 Ma (Tappe *et al.* 2020*a*).

A direct origin of potassic ultramafic magmas from slab remnants, including subducted sedimentary components (Murphy *et al.* 2002; Rapp *et al.* 2008), within the deeper convecting mantle is excluded here. The main reason for this is that the phlogopite/richterite-carbonate bearing peridotitic source assemblages required to explain orangeites and related rocks are largely restricted to the pressure–temperature–fO_2 conditions of the lower cratonic mantle lithosphere (Tappe *et al.* 2007; Foley 2011). Ulmer and Sweeney (2002) pointed out that even under such cratonic mantle conditions, mixed phlogopite/richterite–carbonate assemblages are only metastable and probably do not persist for prolonged periods of geological time. This led Tappe *et al.* (2008) to propose a model in which ancient phlogopite–richterite-bearing cratonic mantle metasomes are fused by small volumes of infiltrating CO_2-rich melts from the underlying asthenosphere, giving rise to K-rich carbonated ultramafic silicate magmas such as aillikites and orangeites.

An inherited subduction signature manifested in cratonic mantle metasomes is supported by $^{40}Ar/^{39}Ar$ age results for phlogopite from strongly metasomatized peridotites along the southern Kaapvaal craton margin, yielding ages of 1.25–1.0 Ga (Hopp *et al.* 2008). In contrast, U–Pb geochronology of zircon in MARID-type xenoliths from the western Kaapvaal craton revealed exclusively Late Mesozoic ages (Konzett *et al.* 1998; Giuliani *et al.* 2015; Hoare *et al.* 2021), but it is uncertain whether these dates represent the timing of K-rich mantle metasomatism or simply the time of isotopic closure as a consequence of lithospheric mantle cooling after a short-lived, yet impactful regional heating event during the Early Mesozoic (Bell *et al.* 2003). Regardless of the timing of lithospheric mantle K-enrichment, it is remarkable how uniform this enriched domain apparently was in terms of its mineralogical and geochemical compositions, as evident from the similar incompatible element systematics (Figs 9–11) and Sr–Nd–Hf isotopic compositions (Figs 12 & 13) of type orangeites. These deep-sourced ultrapotassic magmas erupted in pulses on and off the Kaapvaal craton, across an area that was 1000 × 750 km in size, during progressive breakup of the Gondwana superterrane between 200 and 110 Ma (Tappe *et al.* 2018).

Orangeite v. lamproite terminology: what's in a name?

The potassic ultramafic dykes on the central Kaapvaal craton in South Africa highlight the problems surrounding naming conventions for kimberlites and related rocks. They have been variably referred to as kimberlites, lamprophyres, minettes, lamproites and orangeites (Skinner and Scott 1979; Leeb-Du Toit 1986; Mitchell and Bergman 1991; Mitchell 1995; Gurney and Kirkley 1996; Hammond and Mitchell 2002; McKenna *et al.* 2004; Coe *et al.* 2008), even by the same authors over short periods of time (compare Mitchell and Bergman (1991, p. 72) with Mitchell (1995, p. 30)). There appears to be wide consensus within the alkaline rock petrology community that the term Group 2 kimberlite should be abandoned in favour of these potassic rocks being called orangeites (Mitchell 1995), but in recent years there has been some development to fully assimilate the term orangeite into the lamproite clan. What began with notions about orangeites being the 'lamproite variety Kaapvaal' (Mitchell 2006) has now culminated in orangeites being considered as 'CO_2-rich lamproites' or 'carbonate-rich lamproites' (Pearson *et al.* 2019). This development is regrettable for three main reasons: first, lamproites from classic potassic igneous provinces around the globe are mostly free from primary magmatic carbonate but tend to have a silicate glass matrix instead, such that the term CO_2-rich lamproite presents an oxymoron in a resemblance classification scheme that relies on similarities to standard members (Foley *et al.* 1987). Second, type orangeite from the Kaapvaal craton commonly comprises primitive and evolved varieties, the latter of which may approach CO_2 concentration levels of zero (Fig. 7f) and thus cannot be referred to as CO_2-rich lamproites. Third, the introduction of a carbonate-rich lamproite subgroup obstructs the classification of ultramafic lamprophyres (Tappe *et al.* 2005), because the carbonate-rich lamprophyre variety aillikite would, by the same logic that was applied to type orangeite, also belong to the newly proposed lamproite class. Recently, Sarkar *et al.* (2018) referred to carbonate-rich potassic ultramafic rocks, akin to aillikite or orangeite, as lamproites, which highlights the need for a more coherent classification scheme that can satisfactorily accommodate the petrographical variability of mantle-derived volatile-rich igneous rocks (Mitchell and Tappe 2010).

Here we argue to maintain the status quo of orangeite as a discrete type of mantle-derived potassic magma with occurrences worldwide (Chalapathi Rao *et al.* 2011; Donatti-Filho *et al.* 2013; Kargin *et al.* 2014; Dalton *et al.* 2019; Chalapathi Rao *et al.* 2020; Choi *et al.* 2021; Krmíček *et al*. this volume, in press). The recognition that orangeites *or* Group 2 kimberlites may show closer compositional affinities to cratonic lamproites and aillikites than to archetypal Group 1 kimberlites was a milestone in alkaline rock petrology (Dawson 1987; Mitchell 1995), clearly serving a petrogenetic purpose (Tappe *et al.* 2005). However, modifications of and changes to the terminology of igneous rocks without any obvious advance in our understanding of magma petrogenesis are not endorsed here. Although the names of rocks do not affect what they really are and how they formed – alkaline rock terminology is highly complex and does not appear to benefit from incoherently applied changes – this only complicates matters further.

Conclusions

- The mineralogical and geochemical compositions of 15 individual potassic ultramafic dykes, intersecting the western Bushveld Complex, show that these Mesozoic minor intrusions represent 'typical' Kaapvaal craton orangeites, formerly known as Group 2 kimberlites. A strong olivine control is recognized in the magmatic evolution of the orangeite dykes, with olivine-poor more evolved varieties petrographically resembling lamprophyres. Olivine fractionation and physical sorting are held responsible for the absence of significant quantities of diamond, even though the orangeite magmas traversed one of the richest diamond repositories in the world, as represented by the central Kaapvaal cratonic mantle lithosphere.
- The enriched Sr–Nd–Hf isotopic compositions of the Bushveld-intersecting orangeite dykes suggest a magma origin from ancient K-metasomatized mantle lithosphere, similar to the source of other Kaapvaal craton orangeites. Despite the highly enriched incompatible trace element contents, the orangeite samples studied exhibit pronounced depletions in Th–U–Nb–Ta as well as Ti, resulting in high LILE/HFSE ratios. Such a subduction zone geochemical signature is common among the Mesozoic orangeites from across the Kaapvaal craton. The 'stored' subduction signature is best ascribed to K-rich metasomatism of the cratonic mantle lithosphere in the vicinity of Mesoproterozoic collision zones associated with the Namaqua–Natal orogeny during Rodinia supercontinent formation.
- Our study reinforces that orangeites represent a discrete type of mantle-derived potassic magma. Although compositional similarities with cratonic lamproites and ultramafic lamprophyres do exist, type orangeite from South Africa is sufficiently distinct such that different magma formation processes are implied.

Acknowledgements ST acknowledges financial support by the National Research Foundation of South Africa through the IPRR funding scheme and from the Geological Society of South Africa via 2019–21 REI grants. The Deep and Early Earth Processes Research Group is financially supported by the DSI-NRF CIMERA Center of Excellence. AMS was the recipient of a post-doctoral fellowship co-sponsored by the University of Johannesburg (Faculty of Science award to ST) and the National Research Foundation of South Africa via its SARChI funding scheme (awarded to Fanus Viljoen). We thank Impala Platinum Holdings Limited and Sibanye–Stillwater Limited, in particular David Sharpe and Riana Knipe, for facilitating our sampling campaigns, both underground and in the drillcore archives. Valuable discussions with George Henry, Jan Kramers, David Moate and Anthony Balakrishna are much appreciated. We also thank Christian Reinke (University of Johannesburg) and Heidi Baier (University of Münster) for excellent technical support. Harald Strauss is acknowledged for the CO_2 determinations at the University of Münster, and Armin Zeh for provision of the map used in modified form as our Figure 1. Lastly, Lukas Krmicek and Chalapathi Rao are sincerely thanked for the invitation to contribute to this GSL Special Publication.

Author contributions **ST**: data curation (lead), formal analysis (equal), funding acquisition (lead), investigation (lead), project administration (lead), supervision (lead), writing – original draft (lead), writing – review & editing (lead); **AMS**: formal analysis (equal), investigation (equal), writing – review & editing (supporting); **AHW**: formal analysis (equal), writing – review & editing (supporting); **AS**: formal analysis (equal), writing – review & editing (supporting).

Funding This work was supported by a grant from the National Research Foundation South Africa (CIMERA 1976) to Sebastian Tappe.

Data availability All data generated or analysed during this study are included in this published article (and its supplementary information files).

References

Abersteiner, A., Kamenetsky, V.S. *et al*. 2019. Composition and emplacement of the Benfontein kimberlite sill complex (Kimberley, South Africa): textural, petrographic and melt inclusion constraints. *Lithos*, **324**, 297–314, https://doi.org/10.1016/j.lithos.2018.11.017

Agangi, A., Hofmann, A., Hegner, E., Xie, H.Q., Teschner, C., Slabunov, A. and Svetov, S.A. 2020. The Mesoarchaean Dominion Group and the onset of intracontinental volcanism on the Kaapvaal craton: geological, geochemical and temporal constraints. *Gondwana Research*, **84**, 131–150, https://doi.org/10.1016/j.gr.2020.03.005

Bast, R., Scherer, E.E., Sprung, P., Fischer-Gödde, M., Stracke, A. and Mezger, K. 2015. A rapid and efficient ion-exchange chromatography for Lu–Hf, Sm–Nd, and Rb–Sr geochronology and the routine isotope analysis of sub-ng amounts of Hf by MC–ICP–MS. *Journal of Analytical Atomic Spectrometry*, **30**, 2323–2333, https://doi.org/10.1039/C5JA00283D

Baughman, J.S. and Flowers, R.M. 2020. Mesoproterozoic burial of the Kaapvaal craton, southern Africa during Rodinia supercontinent assembly from (U–Th)/He thermochronology. *Earth and Planetary Science Letters*, **531**, 1–13, https://doi.org/10.1016/j.epsl.2019.115930

Becker, M. and le Roex, A.P. 2006. Geochemistry of South African on- and off-craton, Group I and Group II kimberlites: petrogenesis and source region evolution. *Journal of Petrology*, **47**, 673–703, https://doi.org/10.1093/petrology/egi089

Bell, D.R., Schmitz, M.D. and Janney, P.E. 2003. Mesozoic thermal evolution of the southern African mantle lithosphere. *Lithos*, **71**, 273–287, https://doi.org/10.1016/s0024-4937(03)00117-8

Bouvier, A., Vervoort, J.D. and Patchett, P.J. 2008. The Lu–Hf and Sm–Nd isotopic composition of CHUR: constraints from unequilibrated chondrites and implications for the bulk composition of terrestrial planets. *Earth and Planetary Science Letters*, **273**, 48–57, https://doi.org/10.1016/j.epsl.2008.06.010

Bussweiler, Y., Foley, S.F., Prelevic, D. and Jacob, D.E. 2015. The olivine macrocryst problem: new insights from minor and trace element compositions of olivine from Lac de Gras kimberlites, Canada. *Lithos*, **220**, 238–252, https://doi.org/10.1016/j.lithos.2015.02.016

Byerly, B.L., Lowe, D.R., Drabon, N., Coble, M.A., Burns, D.H. and Byerly, G.R. 2018. Hadean zircon from a 3.3 Ga sandstone, Barberton greenstone belt, South Africa. *Geology*, **46**, 967–970, https://doi.org/10.1130/g45276.1

Cawthorn, R.G., Eales, H.V., Walraven, F., Uken, R. and Watkeys, M.K. 2006. The Bushveld Complex. *In*: Johnson, M.R., Anhaeusser, C.R. and Thomas, R.J. (eds) *The Geology of South Africa*. Geological Society of South Africa and Council for Geoscience, Johannesburg, 261–281.

Chalapathi Rao, N.V., Lehmann, B., Mainkar, D. and Belyatsky, B. 2011. Petrogenesis of the end-Cretaceous diamondiferous Behradih orangeite pipe: implication for mantle plume–lithosphere interaction in the Bastar craton, Central India. *Contributions to Mineralogy and Petrology*, **161**, 721–742, https://doi.org/10.1007/s00410-010-0559-2

Chalapathi Rao, N.V., Giri, R.K., Sharma, A. and Pandey, A. 2020. Lamprophyres from the Indian Shield: a review of their occurrence, petrology, tectonomagmatic significance and relationship with the kimberlites and related rocks. *Episodes*, **43**, 231–248, https://doi.org/10.18814/epiiugs/2020/020014

Chauvel, C., Lewin, E., Carpentier, M., Arndt, N.T. and Marini, J.C. 2008. Role of recycled oceanic basalt and sediment in generating the Hf-Nd mantle array. *Nature Geoscience*, **1**, 64–67, https://doi.org/10.1038/ngeo.2007.51

Choi, E., Fiorentini, M.L., Giuliani, A., Foley, S.F., Maas, R. and Graham, S. 2021. Petrogenesis of Proterozoic alkaline ultramafic rocks in the Yilgarn Craton, Western Australia. *Gondwana Research*, **93**, 197–217, https://doi.org/10.1016/j.gr.2021.01.011

Choudhary, B.R., Santosh, M., Ravi, S. and Babu, E.V.S.S.K. 2020. Spinel and Ti-rich schorlomite from the Wajrakarur kimberlites, southern India: implications for metasomatism, diamond potential and orangeite lineage. *Ore Geology Reviews*, **126**, 1–19, https://doi.org/10.1016/j.oregeorev.2020.103727

Choukroun, M., O'Reilly, S.Y., Griffin, W.L., Pearson, N.J. and Dawson, J.B. 2005. Hf isotopes of MARID (mica–amphibole–rutile–ilmenite–diopside) rutile trace metasomatic processes in the lithospheric mantle. *Geology*, **33**, 45–48, https://doi.org/10.1130/G21084.1

Coe, N., le Roex, A.P., Gurney, J.J., Pearson, D.G. and Nowell, G.M. 2008. Petrogenesis of the Swartruggens and Star Group II kimberlite dyke swarms, South Africa: constraints from whole rock geochemistry. *Contributions to Mineralogy and Petrology*, **156**, 627–652, https://doi.org/10.1007/s00410-008-0305-1

Dalton, H., Giuliani, A., O'Brien, H., Phillips, D., Hergt, J. and Maas, R. 2019. Petrogenesis of a hybrid cluster of evolved kimberlites and ultramafic lamprophyres in the Kuusamo area, Finland. *Journal of Petrology*, **60**, 2025–2050, https://doi.org/10.1093/petrology/egz062

Dawson, J.B. 1987. The kimberlite clan: relationship with olivine and leucite lamproites, and inferences for upper-mantle metasomatism. *In*: Fitton, J.G. and Upton, B.G.J. (eds) *Alkaline igneous rocks*. Geological Society of London, London, 95–101.

Daya, P. 2019. *The petrology and petrogenesis of lamprophyric dykes in the Bushveld Complex, and their possible role in causing gas outbursts*. MSc, University of the Witwatersrand.

Daya, P., Hughes, H.S.R., Bybee, G.M., Kerr, M., Kinnaird, J.A. and Foster, P.J. 2018. Understanding gas explosions in the platinum mines of the Bushveld Complex using applied fluid inclusion and gas chromatography studies. Paper V31I-0237, presented at the *American Geophysical Union, Fall Meeting*, Washington, DC.

de Wit, M.J., Roering, C. *et al*. 1992. Formation of an Archean continent. *Nature*, **357**, 553–562, https://doi.org/10.1038/357553a0

de Wit, M.C.J., Bhebhe, Z. *et al*. 2016. Overview of diamond resources in Africa. *Episodes*, **39**, 199–237, https://doi.org/10.18814/epiiugs/2016/v39i2/95776

Dongre, A. and Tappe, S. 2019. Kimberlite and carbonatite dykes within the Premier diatreme root (Cullinan Diamond Mine, South Africa): new insights to mineralogical-genetic classifications and magma CO_2 degassing. *Lithos*, **338–339**, 155–173, https://doi.org/10.1016/j.lithos.2019.04.020

Dongre, A.N., Viljoen, K.S., Rao, N.V.C. and Gucsik, A. 2016. Origin of Ti-rich garnets in the groundmass of Wajrakarur field kimberlites, southern India: insights from EPMA and Raman spectroscopy. *Mineralogy*

and Petrology, **110**, 295–307, https://doi.org/10.1007/s00710-016-0428-4

Donatti-Filho, J.P., Tappe, S., Oliveira, E.P. and Heaman, L.M. 2013. Age and origin of the Neoproterozoic Brauna kimberlites: Melt generation within the metasomatized base of the São Francisco craton, Brazil. *Chemical Geology*, **353**, 19–35, https://doi.org/10.1016/j.chemgeo.2012.06.004

Field, M., Stiefenhofer, J., Robey, J. and Kurszlaukis, S. 2008. Kimberlite-hosted diamond deposits of southern Africa: a review. *Ore Geology Reviews*, **34**, 33–75, https://doi.org/10.1016/j.oregeorev.2007.11.002

Field, M., Gernon, T.M., Mock, A., Walters, A., Sparks, R.S.J. and Jerram, D.A. 2009. Variations of olivine abundance and grain size in the Snap Lake kimberlite intrusion, Northwest Territories, Canada: a possible proxy for diamonds. *Lithos*, **112**, 23–35, https://doi.org/10.1016/j.lithos.2009.04.019

Fitzpayne, A., Giuliani, A., Maas, R., Hergt, J., Janney, P. and Phillips, D. 2019. Progressive metasomatism of the mantle by kimberlite melts: Sr–Nd–Hf–Pb isotope compositions of MARID and PIC minerals. *Earth and Planetary Science Letters*, **509**, 15–26, https://doi.org/10.1016/j.epsl.2018.12.013

Foley, S.F. 1992. Vein-plus-wall-rock melting mechanism in the lithosphere and the origin of potassic alkaline magmas. *Lithos*, **28**, 435–453, https://doi.org/10.1016/0024-4937(92)90018-T

Foley, S.F. 2011. A reappraisal of redox melting in the Earth's mantle as a function of tectonic setting and time. *Journal of Petrology*, **52**, 1363–1391, https://doi.org/10.1093/petrology/egq061

Foley, S.F. and Wheller, G.E. 1990. Parallels in the origin of the geochemical signatures of island arc volcanics and continental potassic igneous rocks: the role of residual titanates. *Chemical Geology*, **85**, 1–18, https://doi.org/10.1016/0009-2541(90)90120-V

Foley, S.F., Venturelli, G., Green, D.H. and Toscani, L. 1987. The ultrapotassic rocks: characteristics, classification, and constraints for petrogenetic models. *Earth-Science Reviews*, **24**, 81–134, https://doi.org/10.1016/0012-8252(87)90001-8

Fourie, G.P. 1958. The diamond occurrences near Swartruggens, Transvaal. *Geological Survey of South Africa Bulletin*, **26**, 1–16.

Fraser, K.J., Hawkesworth, C.J., Erlank, A.J., Mitchell, R.H. and Scott Smith, B.H. 1985. Sr, Nd and Pb isotope and minor element geochemistry of lamproites and kimberlites. *Earth and Planetary Science Letters*, **76**, 57–70, https://doi.org/10.1016/0012-821X(85)90148-7

Frimmel, H.E., Zeh, A., Lehmann, B., Hallbauer, D. and Frank, W. 2009. Geochemical and geochronological constraints on the nature of the immediate basement next to the Mesoarchaean auriferous Witwatersrand basin, South Africa. *Journal of Petrology*, **50**, 2187–2220, https://doi.org/10.1093/petrology/egp073

Giuliani, A. 2018. Insights into kimberlite petrogenesis and mantle metasomatism from a review of the compositional zoning of olivine in kimberlites worldwide. *Lithos*, **312**, 322–342, https://doi.org/10.1016/j.lithos.2018.04.029

Giuliani, A., Phillips, D. *et al*. 2015. Did diamond-bearing orangeites originate from MARID-veined peridotites in the lithospheric mantle? *Nature Communications*, **6**, 1–10, https://doi.org/10.1038/ncomms7837

Giuliani, A., Phillips, D., Kamenetsky, V.S. and Goemann, K. 2016. Constraints on kimberlite ascent mechanisms revealed by phlogopite compositions in kimberlites and mantle xenoliths. *Lithos*, **240**, 189–201, https://doi.org/10.1016/j.lithos.2015.11.013

Grégoire, M., Bell, D.R. and le Roex, A.P. 2002. Trace element geochemistry of phlogopite-rich mafic mantle xenoliths: their classification and their relationship to phlogopite-bearing peridotites and kimberlites revisited. *Contributions to Mineralogy and Petrology*, **142**, 603–625, https://doi.org/10.1007/s00410-001-0315-8

Griffin, W.L., Pearson, N.J., Belousova, E.A., Jackson, S.E., van Achterbergh, E., O'Reilly, S.Y. and Shee, S.R. 2000. The Hf isotope composition of cratonic mantle: LAM–MC–ICPMS analysis of zircon megacrysts in kimberlites. *Geochimica et Cosmochimica Acta*, **64**, 133–147, https://doi.org/10.1016/S0016-7037(99)00343-9

Griffin, W.L., Batumike, J.M., Greau, Y., Pearson, N.J., Shee, S.R. and O'Reilly, S.Y. 2014. Emplacement ages and sources of kimberlites and related rocks in southern Africa: U–Pb ages and Sr–Nd isotopes of groundmass perovskite. *Contributions to Mineralogy and Petrology*, **168**, 1–13, https://doi.org/10.1007/s00410-014-1032-4

Grunsky, E.C. and Kjarsgaard, B.A. 2008. Classification of distinct eruptive phases of the diamondiferous Star kimberlite, Saskatchewan, Canada based on statistical treatment of whole rock geochemical analyses. *Applied Geochemistry*, **23**, 3321–3336, https://doi.org/10.1016/j.apgeochem.2008.04.027

Gumsley, A., Stamsnijder, J. *et al*. 2020. Neoarchean large igneous provinces on the Kaapvaal craton in southern Africa re-define the formation of the Ventersdorp Supergroup and its temporal equivalents. *Geological Society of America Bulletin*, **132**, 1829–1844, https://doi.org/10.1130/b35237.1

Gurney, J.J. and Kirkley, M.B. 1996. Kimberlite dyke mining in South Africa. *Africa Geoscience Review*, **3**, 191–201.

Hammond, A.L. and Mitchell, R.H. 2002. Accessory mineralogy of orangeite from Swartruggens, South Africa. *Mineralogy and Petrology*, **76**, 1–19, https://doi.org/10.1007/s007100200029

Hoare, B.C., O'Sullivan, G. and Tomlinson, E.L. 2021. Metasomatism of the Kaapvaal Craton during Cretaceous intraplate magmatism revealed by combined zircon U–Pb isotope and trace element analysis. *Chemical Geology*, **578**, 120302, https://doi.org/10.1016/j.chemgeo.2021.120302

Hopp, J., Trieloff, M. *et al*. 2008. Ar-40/Ar-39-ages of phlogopite in mantle xenoliths from South African kimberlites: evidence for metasomatic mantle impregnation during the Kibaran orogenic cycle. *Lithos*, **106**, 351–364, https://doi.org/10.1016/j.lithos.2008.09.001

Howarth, G.H. and Giuliani, A. 2020. Contrasting types of micaceous kimberlite–lamproite magmatism from the Man Craton (West Africa): new insights from petrography and mineral chemistry. *Lithos*, **362**, 105483, https://doi.org/10.1016/j.lithos.2020.105483

Howarth, G.H. and Taylor, L.A. 2016. Multi-stage kimberlite evolution tracked in zoned olivine from the

Benfontein sill, South Africa. *Lithos*, **262**, 384–397, https://doi.org/10.1016/j.lithos.2016.07.028

Howarth, G.H., Skinner, E.M.W. and Prevec, S.A. 2011. Petrology of the hypabyssal kimberlite of the Kroonstad Group II kimberlite (orangeite) cluster, South Africa: evolution of the magma within the cluster. *Lithos*, **125**, 795–808, https://doi.org/10.1016/j.lithos.2011.05.001

Hughes, H.S.R., McDonald, I., Kinnaird, J.A., Nex, P.A.M. and Bybee, G.M. 2016. The metallogenesis of the lithospheric mantle and its bearing on the Bushveld magmatic event: evidence from lamprophyric dykes and critical metals in mantle xenolith sulphides. Presented at the *35th International Geological Congress*, Cape Town, South Africa.

Jacobs, J., Pisarevsky, S., Thomas, R.J. and Becker, T. 2008. The Kalahari Craton during the assembly and dispersal of Rodinia. *Precambrian Research*, **160**, 142–158, https://doi.org/10.1016/j.precamres.2007.04.022

Janse, A.J.A. and Sheahan, P.A. 1995. Catalogue of world wide diamond and kimberlite occurrences: a selective and annotative approach. *Journal of Geochemical Exploration*, **53**, 73–111, https://doi.org/10.1016/0375-6742(94)00017-6

Jaques, A.L. and Foley, S.F. 2018. Insights into the petrogenesis of the West Kimberley lamproites from trace elements in olivine. *Mineralogy and Petrology*, **112**, 519–537, https://doi.org/10.1007/s00710-018-0612-9

Jelsma, H., Barnett, W., Richards, S. and Lister, G. 2009. Tectonic setting of kimberlites. *Lithos*, **112**, 155–165, https://doi.org/10.1016/j.lithos.2009.06.030

Jochum, K.P., Weis, U. *et al*. 2016. Reference values following ISO guidelines for frequently requested rock reference materials. *Geostandards and Geoanalytical Research*, **40**, 333–350, https://doi.org/10.1111/j.1751-908X.2015.00392.x

Kamenetsky, V.S., Kamenetsky, M.B. *et al*. 2008. Olivine in the Udachnaya–East kimberlite (Yakutia, Russia): types, compositions and origins. *Journal of Petrology*, **49**, 823–839, https://doi.org/10.1093/petrology/egm033

Kargin, A.V., Nosova, A.A., Larionova, Y.O., Kononova, V.A., Borisovsky, S.E., Kovalchuk, E.V. and Griboedova, I.G. 2014. Mesoproterozoic orangeites (Kimberlites II) of West Karelia: mineralogy, geochemistry, and Sr–Nd isotope composition. *Petrology*, **22**, 151–183, https://doi.org/10.1134/s0869591114020039

Kjarsgaard, B.A., Pearson, D.G., Tappe, S., Nowell, G.M. and Dowall, D. 2009. Geochemistry of hypabyssal kimberlites from Lac de Gras, Canada: comparisons to a global database and applications to the parent magma problem. *Lithos*, **112**, 236–248, https://doi.org/10.1016/j.lithos.2009.06.001

Klump, J. and Gurney, J.J. 1998. A pilot study of the Swartruggens kimberlite dyke swarm. *International Kimberlite Conference: Extended Abstracts*, **7**, 441–442, https://doi.org/10.29173/ikc2761

Konzett, J., Armstrong, R.A., Sweeney, R.J. and Compston, W. 1998. The timing of MARID metasomatism in the Kaapvaal mantle: an ion probe study of zircons from MARID xenoliths. *Earth and Planetary Science Letters*, **160**, 133–145, https://doi.org/10.1016/S0012-821X(98)00073-9

Korolev, N.M., Kopylova, M.G., Bussweiler, Y., Pearson, D.G., Gurney, J.J. and Davidson, J. 2018. The uniquely high-temperature character of Cullinan diamonds: a signature of the Bushveld mantle plume? *Lithos*, **304**, 362–373, https://doi.org/10.1016/j.lithos.2018.02.011

Kramers, J.D., Roddick, J.C.M. and Dawson, J.B. 1983. Trace element and isotope studies on veined, metasomatic and 'MARID' xenoliths from Bultfontein, South Africa. *Earth and Planetary Science Letters*, **65**, 90–106, https://doi.org/10.1016/0012-821X(83)90192-9

Krmíček, L., Magna, T., Pandey, A., Chalapathi Rao, N.V. and Kynický, J. In press. Lithium isotopes in kimberlites, lamproites and lamprophyres as tracers of source components and processes related to supercontinent cycles. In: Krmíček, L. and Chalapathi Rao, N.V. (eds) *Lamprophyres, Lamproites and Related Rocks: Tracers to Supercontinent Cycles and Metallogenesis*. Geological Society, London, Special Publications, **513**, https://doi.org/10.1144/SP513-2021-60

Kröner, A., Hoffmann, J.E. *et al*. 2019. Archaean crystalline rocks of the eastern Kaapvaal craton. *In*: Kröner, A. and Hofmann, A. (eds) *The Archaean Geology of the Kaapvaal Craton, Southern Africa*. Springer, Heidelberg, 1–32.

Leeb-Du Toit, A. 1986. The Impala Platinum Mines. *In*: Anhaeusser, C.R. and Maske, S. (eds) *Mineral Deposits of Southern Africa*. Geological Society of South Africa, Johannesburg, 1091–1106.

Lerobane, N.M. 2020. *Mineralogy and geochemistry of ultramafic dykes of the western Bushveld Complex (Impala and Lonmin Platinum Mines)*. BS. Honours, University of Johannesburg.

le Roex, A.P., Bell, D.R. and Davis, P. 2003. Petrogenesis of Group I kimberlites from Kimberley, South Africa: evidence from bulk-rock geochemistry. *Journal of Petrology*, **44**, 2261–2286, https://doi.org/10.1093/petrology/egg077

Lugmair, G.W. and Marti, K. 1978. Lunar initial $^{143}Nd/^{144}Nd$: differential evolution of the lunar crust and mantle. *Earth and Planetary Science Letters*, **39**, 349–357, https://doi.org/10.1016/0012-821X(78)90021-3

McKenna, N., Gurney, J.J., Klump, J. and Davidson, J.M. 2004. Aspects of diamond mineralisation and distribution at the Helam Mine, South Africa. *Lithos*, **77**, 193–208, https://doi.org/10.1016/j.lithos.2004.04.004

Mitchell, R.H. 1986. *Kimberlites: Mineralogy, geochemistry and Petrology*. Plenum Press, New York.

Mitchell, R.H. 1995. *Kimberlites, Orangeites, and Related Rocks*. Plenum Press, New York.

Mitchell, R.H. 2006. Potassic magmas derived from metasomatized lithospheric mantle: nomenclature and relevance to exploration for diamond-bearing rocks. *Journal of the Geological Society of India*, **67**, 317–327.

Mitchell, R.H. and Bergman, S.C. 1991. *Petrology of Lamproites*. Plenum Press, New York.

Mitchell, R.H. and Tappe, S. 2010. Discussion of 'Kimberlites and aillikites as probes of the continental lithospheric mantle', by D. Francis and M. Patterson (*Lithos* v. 109, p. 72–80). *Lithos*, **115**, 288–292, https://doi.org/10.1016/j.lithos.2009.10.017

Moate, D.P.T. 2019. *Petrology and geochemistry of ultramafic to mafic dykes at the Lonmin Platinum Mine*

(western Bushveld Complex, South Africa). BSc Honours, University of Johannesburg.

Moss, S., Russell, J.K., Scott Smith, B.H. and Brett, R.C. 2010. Olivine crystal size distributions in kimberlite. *American Mineralogist*, **95**, 527–536, https://doi.org/10.2138/am.2010.3277

Mundl-Petermeier, A., Walker, R.J., Fischer, R.A., Lekic, V., Jackson, M.G. and Kurz, M.D. 2020. Anomalous W-182 in high He-3/He-4 ocean island basalts: fingerprints of Earth's core? *Geochimica et Cosmochimica Acta*, **271**, 194–211, https://doi.org/10.1016/j.gca.2019.12.020

Murphy, D.T., Collerson, K.D. and Kamber, B.S. 2002. Lamproites from Gaussberg, Antarctica: possible transition zone melts of Archaean subducted sediments. *Journal of Petrology*, **43**, 981–1001, https://doi.org/10.1093/petrology/43.6.981

Nasir, S., Al-Khirbash, S. *et al*. 2011. Petrogenesis of early Cretaceous carbonatite and ultramafic lamprophyres in a diatreme in the Batain Nappes, Eastern Oman continental margin. *Contributions to Mineralogy and Petrology*, **161**, 47–74, https://doi.org/10.1007/s00410-010-0521-3

Ngwenya, N.S. and Tappe, S. 2021. Diamondiferous lamproites of the Luangwa Rift in central Africa and links to remobilized cratonic lithosphere. *Chemical Geology*, **568**, 120019, https://doi.org/10.1016/j.chemgeo.2020.120019

Nielsen, T.F.D., Jensen, S.M., Secher, K. and Sand, K.K. 2009. Distribution of kimberlite and aillikite in the Diamond Province of southern West Greenland: a regional perspective based on groundmass mineral chemistry and bulk compositions. *Lithos*, **112**, 358–371, https://doi.org/10.1016/j.lithos.2009.05.035

Nowell, G.M., Pearson, D.G., Bell, D.R., Carlson, R.W., Smith, C.B., Kempton, P.D. and Noble, S.R. 2004. Hf isotope systematics of kimberlites and their megacrysts: new constraints on their source regions. *Journal of Petrology*, **45**, 1583–1612, https://doi.org/10.1093/petrology/egh024

Palme, H. and Jones, A. 2003. Solar system abundances of the elements. *In*: Carlson, R.W. (ed.) *Treatise on Geochemistry*. Elsevier, Amsterdam, 41–61.

Palme, H. and O'Neill, H.S.C. 2003. Cosmochemical estimates of mantle composition. *In*: Carlson, R.W. (ed.) *Treatise on Geochemistry*. Elsevier, Amsterdam, 1–38.

Pearce, J.A. and Peate, D.W. 1995. Tectonic implications of the composition of volcanic arc magmas. *Annual Review of Earth and Planetary Sciences*, **23**, 251–285, https://doi.org/10.1146/annurev.earth.23.1.251

Pearson, D.G., Woodhead, J. and Janney, P.E. 2019. Kimberlites as geochemical probes of Earth's mantle. *Elements*, **15**, 387–392, https://doi.org/10.2138/gselements.15.6.387

Peccerillo, R. and Taylor, S.R. 1976. Geochemistry of Eocene calc-alkaline volcanic rocks from the Kastamonu area, northern Turkey. *Contributions to Mineralogy and Petrology*, **58**, 63–81, https://doi.org/10.1007/BF00384745

Phillips, D., Machin, K.J., Kiviets, G.B., Fourie, L.F., Roberts, M.A. and Skinner, E.M.W. 1998. A petrographic and $^{40}Ar/^{39}Ar$ geochronological study of the Voorspoed kimberlite, South Africa: implications for the origin of Group II kimberlite magmatism. *South African Journal of Geology*, **101**, 299–306.

Poujol, M., Robb, L.J., Anhaeusser, C.R. and Gericke, B. 2003. A review of the geochronological constraints on the evolution of the Kaapvaal Craton, South Africa. *Precambrian Research*, **127**, 181–213, https://doi.org/10.1016/s0301-9268(03)00187-6

Prelevic, D. and Foley, S.F. 2007. Accretion of arc-oceanic lithospheric mantle in the Mediterranean: evidence from extremely high-Mg olivines and Cr-rich spinel inclusions in lamproites. *Earth and Planetary Science Letters*, **256**, 120–135, https://doi.org/10.1016/j.epsl.2007.01.018

Prelevic, D., Foley, S.F. and Jacob, D. 2013. Recycling plus: a new recipe for the formation of Alpine-Himalayan orogenic mantle lithosphere. *Earth and Planetary Science Letters*, **362**, 187–197, https://doi.org/10.1016/j.epsl.2012.11.035

Rapp, R.P., Irifune, T., Shimizu, N., Nishiyama, N., Norman, M.D. and Inoue, J. 2008. Subduction recycling of continental sediments and the origin of geochemically enriched reservoirs in the deep mantle. *Earth and Planetary Science Letters*, **271**, 14–23, https://doi.org/10.1016/j.epsl.2008.02.028

Rizo, H., Andrault, D. *et al*. 2019. W-182 evidence for core-mantle interaction in the source of mantle plumes. *Geochemical Perspectives Letters*, **11**, 6–11, https://doi.org/10.7185/geochemlet.1917

Rock, N.M.S. 1991. *Lamprophyres*. Blackie & Son, Glasgow.

Roeder, P.L. and Schulze, D.J. 2008. Crystallization of groundmass spinel in kimberlite. *Journal of Petrology*, **49**, 1473–1495, https://doi.org/10.1093/petrology/egn034

Rooney, T.O., Girard, G. and Tappe, S. 2020. The impact on mantle olivine resulting from carbonated silicate melt interaction. *Contributions to Mineralogy and Petrology*, **175**, 1–15, https://doi.org/10.1007/s00410-020-01694-0

Roy, P., Balaram, V., Kumar, A., Satyanarayanan, M. and Rao, T.G. 2007. New REE and trace element data on two kimberlitic reference materials by ICP–MS. *Geostandards and Geoanalytical Research*, **31**, 261–273, https://doi.org/10.1111/j.1751-908X.2007.00836.x

Sarkar, C., Storey, C.D. and Hawkesworth, C.J. 2014. Using perovskite to determine the pre-shallow level contamination magma characteristics of kimberlite. *Chemical Geology*, **363**, 76–90, https://doi.org/10.1016/j.chemgeo.2013.10.032

Sarkar, C., Kjarsgaard, B.A., Pearson, D.G., Heaman, L.M., Locock, A.J. and Armstrong, J.P. 2018. Geochronology, classification and mantle source characteristics of kimberlites and related rocks from the Rae Craton, Melville Peninsula, Nunavut, Canada. *Mineralogy and Petrology*, **112**, 653–672, https://doi.org/10.1007/s00710-018-0632-5

Scherer, E.E., Münker, C. and Mezger, K. 2001. Calibration of the lutetium–hafnium clock. *Science*, **293**, 683–687, https://doi.org/10.1126/science.1061372

Schmitz, M.D., Bowring, S.A., de Wit, M.J. and Gartz, V. 2004. Subduction and terrane collision stabilize the western Kaapvaal craton tectosphere 2.9 billion years ago. *Earth and Planetary Science Letters*, **222**, 363–376, https://doi.org/10.1016/j.epsl.2004.03.036

Shaikh, A.M., Patel, S.C., Bussweiler, Y., Kumar, S.P., Tappe, S., Ravi, S. and Mainkar, D. 2019. Olivine trace element compositions in diamondiferous lamproites from India: proxies for magma origins and the nature of the lithospheric mantle beneath the Bastar and Dharwar cratons. *Lithos*, **324–325**, 501–518, https://doi.org/10.1016/j.lithos.2018.11.026

Shirey, S.B., Harris, J.W. *et al*. 2002. Diamond genesis, seismic structure, and evolution of the Kaapvaal-Zimbabwe craton. *Science*, **297**, 1683–1686, https://doi.org/10.1126/science.1072384

Skinner, E.M.W. 1989. Contrasting Group I and Group II kimberlite petrology: towards a genetic model for kimberlites. *In*: Ross, J. (ed.) *Kimberlites and related rocks*. Geological Society of Australia, Sydney, N.S.W., Australia, 528–544.

Skinner, E.M.W. and Scott, B.H. 1979. Petrography, mineralogy and geochemistry of kimberlites and associated lamprophyre dykes near Swartruggens, Western Transvaal, RSA. *2nd Kimberlite Symposium*, Cambridge, **2**, 1–6.

Smart, K.A., Tappe, S., Stern, R.A., Webb, S.J. and Ashwal, L.D. 2016. Early Archaean tectonics and mantle redox recorded in Witwatersrand diamonds. *Nature Geoscience*, **9**, 255–259, https://doi.org/10.1038/ngeo2628

Smart, K.A., Tappe, S., Ishikawa, A., Pfänder, J.A. and Stracke, A. 2019. K-rich hydrous mantle lithosphere beneath the Ontong Java Plateau: significance for the genesis of oceanic basalts and Archean continents. *Geochimica Et Cosmochimica Acta*, **248**, 311–342, https://doi.org/10.1016/j.gca.2019.01.013

Smart, K.A., Tappe, S., Woodland, A.B., Harris, C., Corcoran, L. and Simonetti, A. 2021. Metasomatized eclogite xenoliths from the central Kaapvaal craton as probes of a seismic mid-lithospheric discontinuity. *Chemical Geology*, **578**, 120286, https://doi.org/10.1016/j.chemgeo.2021.120286

Smith, C.B. 1983. Pb, Sr and Nd isotopic evidence for sources of southern African Cretaceous kimberlites. *Nature*, **304**, 51–54, https://doi.org/10.1038/304 051a0

Smith, C.B., Gurney, J.J., Skinner, E.M.W., Clement, C.R. and Ebrahim, N. 1985. Geochemical character of Southern African kimberlites: a new approach based on isotopic constraints. *Transactions of the Geological Society of South Africa*, **88**, 267–280.

Spencer, C.J., Thomas, R.J., Roberts, N.M.W., Cawood, P.A., Millar, I. and Tapster, S. 2015. Crustal growth during island arc accretion and transcurrent deformation, Natal Metamorphic Province, South Africa: new isotopic constraints. *Precambrian Research*, **265**, 203–217, https://doi.org/10.1016/j.precamres.2015.05.011

Stracke, A. 2012. Earth's heterogeneous mantle: a product of convection-driven interaction between crust and mantle. *Chemical Geology*, **330–331**, 274–299, https://doi.org/10.1016/j.chemgeo.2012.08.007

Tappe, S., Jenner, G.A., Foley, S.F., Heaman, L.M., Besserer, D., Kjarsgaard, B.A. and Ryan, B. 2004. Torngat ultramafic lamprophyres and their relation to the North Atlantic Alkaline Province. *Lithos*, **76**, 491–518, https://doi.org/10.1016/j.lithos.2004.03.040

Tappe, S., Foley, S.F., Jenner, G.A. and Kjarsgaard, B.A. 2005. Integrating ultramafic lamprophyres into the IUGS classification of igneous rocks: rational and implications. *Journal of Petrology*, **46**, 1893–1900, https://doi.org/10.1093/petrology/egi039

Tappe, S., Foley, S.F. *et al*. 2006. Genesis of ultramafic lamprophyres and carbonatites at Aillik Bay, Labrador: a consequence of incipient lithospheric thinning beneath the North Atlantic craton. *Journal of Petrology*, **47**, 1261–1315, https://doi.org/10.1093/petrology/egl008

Tappe, S., Foley, S.F., Stracke, A., Romer, R.L., Kjarsgaard, B.A., Heaman, L.M. and Joyce, N. 2007. Craton reactivation on the Labrador Sea margins: $^{40}Ar/^{39}Ar$ age and Sr–Nd–Hf–Pb isotope constraints from alkaline and carbonatite intrusives. *Earth and Planetary Science Letters*, **256**, 433–454, https://doi.org/10.1016/j.epsl.2007.01.036

Tappe, S., Foley, S.F., Kjarsgaard, B.A., Romer, R.L., Heaman, L.M., Stracke, A. and Jenner, G.A. 2008. Between carbonatite and lamproite: diamondiferous Torngat ultramafic lamprophyres formed by carbonate-fluxed melting of cratonic MARID-type metasomes. *Geochimica Et Cosmochimica Acta*, **72**, 3258–3286, https://doi.org/10.1016/j.gca.2008.03.008

Tappe, S., Steenfelt, A., Heaman, L.M. and Simonetti, A. 2009. The newly discovered Jurassic Tikiusaaq carbonatite-aillikite occurrence, West Greenland, and some remarks on carbonatite–kimberlite relationships. *Lithos*, **112**, 385–399, https://doi.org/10.1016/j.lithos.2009.03.002

Tappe, S., Pearson, D.G., Nowell, G.M., Nielsen, T.F.D., Milstead, P. and Muehlenbachs, K. 2011. A fresh isotopic look at Greenland kimberlites: cratonic mantle lithosphere imprint on deep source signal. *Earth and Planetary Science Letters*, **305**, 235–248, https://doi.org/10.1016/j.epsl.2011.03.005

Tappe, S., Kjarsgaard, B.A., Kurszlaukis, S., Nowell, G.M. and Phillips, D. 2014. Petrology and Nd–Hf isotope geochemistry of the Neoproterozoic Amon kimberlite sills, Baffin Island (Canada): evidence for deep mantle magmatic activity linked to supercontinent cycles. *Journal of Petrology*, **55**, 2003–2042, https://doi.org/10.1093/petrology/egu048

Tappe, S., Romer, R.L., Stracke, A., Steenfelt, A., Smart, K.A., Muehlenbachs, K. and Torsvik, T.H. 2017. Sources and mobility of carbonate melts beneath cratons, with implications for deep carbon cycling, metasomatism and rift initiation. *Earth and Planetary Science Letters*, **466**, 152–167, https://doi.org/10.1016/j.epsl.2017.03.011

Tappe, S., Smart, K.A., Torsvik, T.H., Massuyeau, M. and de Wit, M.C.J. 2018. Geodynamics of kimberlites on a cooling Earth: clues to plate tectonic evolution and deep volatile cycles. *Earth and Planetary Science Letters*, **484**, 1–14, https://doi.org/10.1016/j.epsl.2017.12.013

Tappe, S., Stracke, A., van Acken, D., Strauss, H. and Luguet, A. 2020*a*. Origins of kimberlites and carbonatites during continental collision – insights beyond decoupled Nd–Hf isotopes. *Earth-Science Reviews*, **208**, 103287, https://doi.org/10.1016/j.earscirev.2020.103287

Tappe, S., Budde, G., Stracke, A., Wilson, A. and Kleine, T. 2020*b*. The tungsten-182 record of kimberlites above the African superplume: exploring links to the core-mantle boundary. *Earth and Planetary Science*

Letters, **547**, 116473, https://doi.org/10.1016/j.epsl.2020.116473

Ulmer, P. and Sweeney, R.J. 2002. Generation and differentiation of Group II kimberlites: constraints from a high-pressure experimental study to 10 GPa. *Geochimica Et Cosmochimica Acta*, **66**, 2139–2153, https://doi.org/10.1016/S0016-7037(02)00898-0

Van Schijndel, V., Cornell, D.H., Anczkiewicz, R. and Schersten, A. 2020. Evidence for Mesoproterozoic collision, deep burial and rapid exhumation of garben-schiefer in the Namaqua Front, *South Africa Geoscience Frontiers*, **11**, 511–531, https://doi.org/10.1016/j.gsf.2019.06.004

Viljoen, K.S., Dobbe, R., Smit, B., Thomassot, E. and Cartigny, P. 2004. Petrology and geochemistry of a diamondiferous lherzolite from the Premier diamond mine, South Africa. *Lithos*, **77**, 539–552, https://doi.org/10.1016/j.lithos.2004.03.023

Wagner, P.A. 1914. *The Diamond Fields of South Africa*. Transvaal Leader, Johannesburg.

Wilson, A.H. 2012. A chill sequence to the Bushveld Complex: insight into the first stage of emplacement and implications for the parental magmas. *Journal of Petrology*, **53**, 1123–1168, https://doi.org/10.1093/petrology/egs011

Zeh, A., Ovtcharova, M., Wilson, A.H. and Schaltegger, U. 2015. The Bushveld Complex was emplaced and cooled in less than one million years: results of zirconology, and geotectonic implications. *Earth and Planetary Science Letters*, **418**, 103–114, https://doi.org/10.1016/j.epsl.2015.02.035

Zeh, A., Wilson, A.H., Gudelius, D. and Gerdes, A. 2019. Hafnium isotopic composition of the Bushveld Complex requires mantle melt–upper crust mixing: new evidence from zirconology of mafic, felsic and metasedimentary rocks. *Journal of Petrology*, **60**, 2169–2200, https://doi.org/10.1093/petrology/egaa004

Zurevinski, S.E. and Mitchell, R.H. 2011. Highly evolved hypabyssal kimberlite sills from Wemindji, Quebec, Canada: insights into the process of flow differentiation in kimberlite magmas. *Contributions to Mineralogy and Petrology*, **161**, 765–776, https://doi.org/10.1007/s00410-010-0561-8